Chapter 6
Backscattering Data

In Sects. 6.1–6.8 we describe results of [115]. As to the numerical results of Sect. 6.8, Figs. 6.2a, b were published in *Methods and Applications of Analysis* [116] and are reprinted with permission. Other figures of this chapter were not published elsewhere.

6.1 Introduction

In Chaps. 2–5 we have considered the case of the so-called "complete data". In other words, the data were given at the entire boundary of the domain of interest. In the case of the experimental data of Chap. 5 only transmitted data were given, although they were measured on the transmitted side only and only for a very narrow view angle. Thus, we have worked with incomplete data in Chap. 5. However, the most interesting case of incomplete data is the case when they are given at the backscattering side of the medium. The case of the backscattering data is especially interesting in military applications. In this chapter we model the most suitable arrangement for this case, which is to use a single position of the point source and to measure only the backscattering signal. The target application of this chapter is in imaging of plastic antipersonnel land mines.

In the case of backscattering data, we have both Dirichlet and Neumann boundary conditions at the backscattering part of the boundary. These are informative conditions, since they depend on the unknown coefficient. The Dirichlet boundary condition models the result of measurements. The Neumann boundary condition can be calculated, as soon as the Dirichlet condition is known. As to the rest of the boundary, we have only the radiation condition. This one is a noninformative boundary condition since it is independent on the unknown coefficient. Hence, we use this noninformative condition only for a better stability of our algorithm.

Because of the overdetermination in the boundary conditions on the backscattering side, the idea is to use the quasi-reversibility method (QRM). Hence, the major part of this chapter is devoted to the version of the approximately globally

L. Beilina and M.V. Klibanov, *Approximate Global Convergence and Adaptivity for Coefficient Inverse Problems*, DOI 10.1007/978-1-4419-7805-9_6,

convergent method for the case when the QRM solves (2.49) for functions $q_{n,i}$ (Sect. 2.6.1). Theorem 6.7 is the central theorem of this chapter. Remarks 2.9.4 can be reformulated for this case. In addition, we present in this chapter our most recent computational result. In this result, only the Dirichlet boundary condition is used on the backscattering side of the boundary, and the zero Dirichlet boundary condition for functions $q_{n,i}$ is assigned on the rest of the boundary. With reference to the QRM, we present analytical results of [115] as well as some numerical results in 2D and 3D cases. In particular, the 2D computational result was published in [116]. The 3D result of this chapter was not published before. Computations in 2D were carried out by Dr. Andrey V. Kuzhuget with a help from both authors of this book, and the 3D result was computed by Dr. Natee Pantong with a help from both A.V. Kuzhuget and the second author.

In Sect. 6.9, we present results of our work with **blind** experimental data, which were collected by a forward looking radar of the US Army Research Laboratory (ARL); see [126] for a description of this radar. The ARL data were kindly provided to us, along with the permission to use in this book, by Drs. Lam Nguyen and Anders Sullivan, who work for ARL. The corresponding joint work is [117]. The ARL data were collected in the field, unlike the experimental data of Chap. 5, which were collected in a laboratory. Computations for this case were performed by Dr. A. V. Kuzhuget with a help from the authors of this book.

Because of the structure of these experimental data, only 1D inverse algorithms have a chance to succeed in this case; see Sect. 6.9.2. Thus, we have applied the 1D version of our algorithm [114]. The 1D version of our approximately globally convergent numerical method was initially considered in [114] "only as a preliminary step before applying similar ideas to 2D and 3D cases" (see p. 125 of [114]). This version is based on some approximations, similar with ones of Sect. 6.6.2. On the other hand, 1D numerical methods of [40, 47, 51, 56, 90] do not use approximations like ours, and they also do not need a priori given good first guess for the solution. Our experimental data have a number of uncertainties listed in Sect. 6.9.4. One of examples of such an uncertainty is the 1D modeling of the 3D process. Hence, because of these uncertainties, it is yet unclear how techniques of [40, 47, 51, 56, 90] would perform for these experimental data. The question of comparison of the performance of some of these algorithms with ours for our experimental data is outside of the scope of the current book.

The QRM was first proposed by R. Lattes and J.-L. Lions in their joint book [121]. Carleman estimates were not used for the convergence analysis in this book. It was shown later in [105] that the tool of Carleman estimates is a quite suitable one for proofs of convergence theorems for the QRM. The latter tool was used in a number of publications since then, where analytical results for the QRM were combined with computational ones; see, for example, [49, 59, 102, 106–108].

The QRM is designed to find approximate solutions of ill-posed problems for PDEs, for example, Cauchy problem for the Laplace equation. In particular, it can handle boundary value problems for PDEs with overdetermined boundary conditions, and the backscattering data indeed generate this problem for each

function $q_{n,i}$ in (2.49). The QRM minimizes the Tikhonov functional. However, instead of the traditionally case of a continuous operator, the Tikhonov functional for the QRM is generated by the linear operator of the corresponding PDE, and this operator is unbounded of course. A good feature of the QRM is that the uniqueness and existence of the minimizer (i.e., the regularized solution) for this case follows immediately from the Riesz theorem. However, the question of convergence of regularized solutions to the exact one is much more delicate, and it is usually addressed via a Carleman estimate.

While the QRM was applied only to linear problems in [49,59,102,106–108], our CIP is nonlinear. This causes the major difficulty, compared with previous works. Indeed, the QRM is applied only once in the linear case. Unlike this, we need to apply the QRM on each iteration. However, these iterations cause significant new difficulties in the convergence analysis. Addressing these difficulties is the major new point of the convergence analysis of this chapter.

6.2 Forward and Inverse Problems

First, we pose the forward and inverse problems. Below, $x = (x_1, x_2, x_3) \in \mathbb{R}^3$. The forward problem is the same as the problem (2.1) and (2.2) in Sect. 2.1:

$$c(x) u_{tt} = \Delta u \text{ in } \mathbb{R}^3 \times (0, \infty), \tag{6.1}$$

$$u(x, 0) = 0, u_t(x, 0) = \delta(x - x_0). \tag{6.2}$$

We impose the same conditions on the coefficient $c(x)$ as (2.3), (2.4) in Sect. 2.1, except that we require a little bit higher smoothness. Let $\Omega \subset \mathbb{R}^3$ be a convex bounded domain with the piecewise smooth boundary $\partial\Omega$. We assume that

$$c(x) \in [1, d], \ c(x) = 1 \text{ for } x \in \mathbb{R}^3 \backslash \Omega, \tag{6.3}$$

$$c(x) \in C^4\left(\mathbb{R}^3\right). \tag{6.4}$$

Everywhere below, $\alpha = \text{const.} \in (0, 1)$. It is convenient for our derivations to introduce the following set $\mathbb{M}$ of functions:

$$\mathbb{M} = \left\{c \in C^{\alpha}\left(\mathbb{R}^3\right) : \text{conditions (6.3) hold}\right\}. \tag{6.5}$$

To simplify the presentation and also because of our target application, we now specify the domain $\Omega \subset \mathbb{R}^3$ as follows; see Fig. 6.1. Let $P > 0$ be a constant. Below,

$$\Omega = \{x : -P < x_1, x_2 < P, x_3 \in (0, 2P)\}, \partial\Omega = \cup_{i=1}^{3} \Gamma_i, \tag{6.6}$$

$$\Gamma_1 = \{x : -P < x_1, x_2 < P, x_3 = 0\}, \tag{6.7}$$

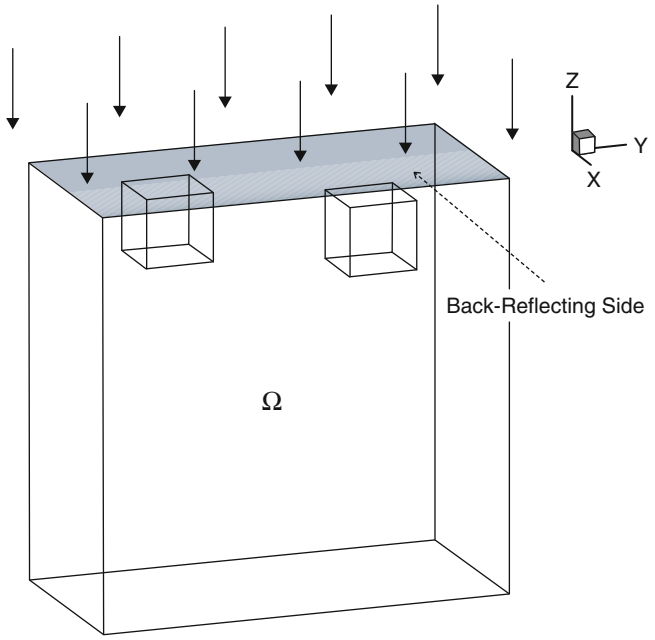

Fig. 6.1 Schematic diagram of data collection in the backscattering case. The incident plane wave falls from the top, and the back reflected data are collected on the top boundary as well

$$\Gamma_2 = \{x : x_1, x_2 = \pm P, x_3 \in (0, 2P)\}, \tag{6.8}$$

$$\Gamma_3 = \{x : -P < x_1, x_2 < P, x_3 = 2P\}. \tag{6.9}$$

Coefficient Inverse Problem 6.2. *Suppose that the coefficient $c(x)$ in (6.1) satisfies conditions (6.3), (6.4) and is unknown in the domain Ω. Determine the coefficient $c(x)$ for $x \in \Omega$, assuming that the following functions $g_0(x,t)$ and $g_1(x,t)$ are known for a single source position $x_0 \in \{x_3 < 0\}$:*

$$u(x,t)|_{\Gamma_1} = g_0(x,t),\ u_{x_3}(x,t)|_{\Gamma_1} = g_1(x,t), t \in (0,\infty). \tag{6.10}$$

Since $x_0 \in \{x_3 < 0\}$, then it follows from (6.6), (6.7), (6.8), and (6.9) that Γ_1 is the backscattering side. Hence, (6.10) models measurements of the backscattering data. In experiments, usually only the function $g_0(x,t)$ is measured. One can approximately assume that this function is known at the entire plane $\{x_3 = 0\}$. Next, since by (6.3) and (6.6) the coefficient $c(x) = 1$ for $x_3 < 0$, then solving the forward problem (6.1), (6.2) in the half space $\{z < 0\}$ with the boundary condition $u(x,t)\ |_{x_3=0} = g_0(x,t)$, one can uniquely determine the function $u(x,t)$ for $x_3 < 0, t > 0$, which gives the function $g_1(x,t)$.

6.3 Laplace Transform

In the case of the backscattering data, we work with an analog of the algorithm of Sect. 2.6.1. An essential difference, however, is that two boundary conditions (6.10) generate overdetermined boundary conditions for functions $q_{n,i}$ in (2.49). This overdetermination, in turn leads to the QRM. To derive (2.49), we have performed in Sect. 2.3 the Laplace transform (2.10) first. Thus, consider the function w defined by

$$w(x,s) = \int_0^\infty u(x,t)\mathrm{e}^{-st}\mathrm{d}t, \text{ for } s \geq \underline{s} = \text{const.} > 0, \tag{6.11}$$

where $\underline{s} > 0$ is a certain number. In our numerical studies, we choose $\underline{s}$ experimentally. We call the parameter s *pseudo-frequency*. The function w satisfies the following conditions:

$$\Delta w - s^2 c(x) w = -\delta(x - x_0), \ x \in \mathbb{R}^3, \forall s \geq \underline{s}, \tag{6.12}$$

$$\lim_{|x|\to\infty} w(x,s) = 0, \forall s \geq \underline{s}. \tag{6.13}$$

The condition (6.13) for sufficiently large $\underline{s} = \underline{s}(c)$ was established in Theorem 2.7.1 Theorem 2.7.2 provides more properties of the solution of the problem (6.12), (6.13). In particular, it follows from this theorem that if $c \in \mathbb{M}$, where the set $\mathbb{M}$ is defined in (6.5), then for every $s > 0$, there exists unique solution w of the problem (6.12), (6.13) of the form

$$w = w_1 + \overline{w}, \text{ where } \overline{w} \in C^{2+\gamma}\left(\mathbb{R}^3\right), \tag{6.14}$$

$$w_1(x,s) = \frac{\exp(-s|x - x_0|)}{4\pi|x - x_0|}. \tag{6.15}$$

The function w_1 solves the problem (6.12), (6.13) for the case $c(x) \equiv 1$.

Having the data at only one side Γ_1 of the cube Ω is not sufficient for a good stability of the numerical solution. To provide a better stability, we now derive an approximate boundary condition for the function $\ln w$ at the rest $\Gamma_2 \cup \Gamma_3$ of the boundary $\partial\Omega$. It follows from (6.15) and (2.101) that the function w satisfies the radiation condition at the infinity, $\lim_{|x|\to\infty}\left(\partial_{|x|}w + sw\right)(x) = 0$, where $\partial_{|x|}w := \partial_r w$ is understood in terms of spherical coordinates with the radius $r := |x - x_0|$. Hence, assuming that the number P in (6.6)–(6.9) is sufficiently large, we impose the following *approximate* boundary condition at $\Gamma_2 \cup \Gamma_3$L:

$$(\partial_n w + sw)|_{\Gamma_2\cup\Gamma_3} = 0. \tag{6.16}$$

It follows from (6.16) that

$$\partial_n(\ln w(x,s))|_{\Gamma_2\cup\Gamma_3} = -s. \tag{6.17}$$

Actually, condition (6.17) is not an informative one. This is because it is independent on the target coefficient $c(x)$. Hence, it is logical to use (6.17) only for a better stability of the algorithm.

We have verified the *approximate* boundary condition (6.16) computationally, both in 3D and 2D cases, as follows. For a variety of cases modeling our target application to imaging of antipersonnel plastic land mines (Sect. 6.1), we have computationally solved the forward problem for (6.12) in a domain $\widehat{\Omega}$, which was much larger than the domain Ω in (6.6), $\Omega \subset \widehat{\Omega}, \partial\Omega \cap \partial\widehat{\Omega} = \varnothing$. Because of (6.13), we have imposed the zero Dirichlet boundary condition at $\partial\widehat{\Omega}$. Next, we have solved (6.12) in the domain Ω with the boundary condition (6.16) at $\Gamma_2 \cup \Gamma_3$. As to Γ_1, we have used the Dirichlet boundary condition, which was calculated from the above solution of the forward problem in $\widehat{\Omega}$. When doing so, we have used the same values of the parameter s for which we have numerically solved our inverse problem. Comparison of these two solutions has consistently revealed that in a subdomain $\widetilde{\Omega} \subset \Omega$, whose boundary had a small distance from $\Gamma_2 \cup \Gamma_3$, these two solutions have almost coincided. Thus, the above provides a numerical justification for the approximation (6.16).

Remark 6.3. A heuristic explanation of a low sensitivity of the function $w(x,s)$ to the choice of boundary conditions at $\Gamma_2 \cup \Gamma_3$ is the following. Consider two arbitrary points $x_1 \neq x_0$ and $x_2 \neq x_0$ with $|x_2 - x_0| > |x_1 - x_0|$. Then, the function

$$f(x_2, s) = \frac{w_1(x_2, s)}{w_1(x_1, s)}$$

decays exponentially as $|x_2 - x_1| \to \infty$, and the point x_1 is fixed. In terms of practical computations of the CIP 6.2, this means that one can use such a boundary condition for the function w at $\Gamma_2 \cup \Gamma_3$ which provides best computational results. On the other hand, this condition will always be a noninformative one. We also refer to Chap. 5 for an analogy, since we have assigned in this chapter a noninformative boundary condition to those five sides of the prism Ω where experimental data were not collected.

6.4 The Algorithm

6.4.1 Preliminaries

The algorithm is similar with the algorithm of Sect. 2.6.1. Therefore, we are rather brief in Sects. 6.4.1 and 6.4.2. However, an essential difference is in the method of solving of (2.49). Indeed, while the problem (2.49), (2.50) is the Dirichlet boundary value problem, which we solve via the FEM, in the case of backscattering data,

(2.50) is replaced with overdetermined boundary conditions. The overdetermination is generated by two functions $g_0(x,t)$ and $g_1(x,t)$ instead of just one in (2.5) for the coefficient inverse problem 2.1.

Quite often, in applications, one can assume that actually, the coefficient $c(x) = 1$ for $x \in \mathbb{R}^3 \backslash G$ where $G \subset \Omega$ is such a subdomain of Ω which is a little bit smaller than the domain of interest Ω. We are doing this here for the sake of convenience of the convergence analysis. Let $P_2 = \text{const.} \in (0, P)$. Denote $\Omega_{P_2} = \Omega \cap \{x_3 \in (0, P_2)\}$. We assume below that $c(x) = 1$, $\forall x \in \mathbb{R}^3 \backslash \Omega_{P_2}$. Consider a subdomain $\Omega' \subset \Omega_{P_2}$ with $\partial\Omega' \cap \partial\Omega_{P_2} = \varnothing$. Choose a function $\chi_1(x) \in C^3\left(\mathbb{R}^3\right)$ such that

$$\chi_1(x) = \begin{cases} 1 \text{ in } \Omega', \\ \text{between 0 and 1 in } \Omega_{P_2} \backslash \Omega', \\ 0 \text{ outside of } \Omega_{P_2}. \end{cases}$$

Next, let $\chi_2(x)$ be the characteristic function of the domain Ω_{P_2}:

$$\chi_2(x) = \begin{cases} 1 \text{ in } \Omega_{P_2}, \\ 0 \text{ outside of } \Omega_{P_2}. \end{cases}$$

Let $c_{n,k}(x)$, $x \in \Omega$ be the function reconstructed by the algorithm described below. Then, by (6.34) and (6.35),

$$c_{n,k} \in [1, d], \ c_{n,k} \in C^{\gamma}\left(\overline{\Omega}\right). \tag{6.18}$$

Similarly with Sect. 2.6, we extend the function $c_{n,i}(x)$ in the entire space $\mathbb{R}^3$ as

$$\widehat{c}_{n,k}(x) := (1 - \chi_1(x)) + \chi_1(x)\, c_{n,k}(x), \forall x \in \mathbb{R}^3. \tag{6.19}$$

Then it follows from (6.5), (6.18), and (6.19) that

$$\widehat{c}_{n,k} \in \mathbb{M}. \tag{6.20}$$

We work below only with the function $w(x,s), s > 0$. Let in (6.12) the coefficient $c \in \mathbb{M}$. Then Theorem 2.7.2 implies that there exists unique solution $w(x,s)$ of the problem (6.12), (6.13) satisfying conditions (6.14) and (6.15). Furthermore, $w(x,s) > 0$ for $x \neq x_0$. Hence, similarly with Sect. 2.3, we consider functions $v(x,s), q(x,s)$ defined as

$$v(x,s) = \frac{\ln w(x,s)}{s^2}, \ q(x,s) = \frac{\partial v(x,s)}{\partial s}. \tag{6.21}$$

Hence,

$$\Delta v + s^2 (\nabla v)^2 = c(x), \ x \in \Omega. \tag{6.22}$$

Assume that we work on the interval $s \in [\underline{s}, \overline{s}]$. Hence,

$$v(x,s) = -\int_s^{\overline{s}} q(x,\tau)\, d\tau + V(x),$$

$$V(x) := V(x,\overline{s}) = \frac{\ln w(x,\overline{s})}{\overline{s}^2}, \tag{6.23}$$

where $V(x)$ is the tail function. Assuming that conditions of Lemma 2.3 hold, we have the asymptotic behavior similar with the one of Sect. 2.3:

$$\|V(x,\overline{s})\|_{C^{2+\gamma}(\overline{\Omega})} = O\left(\frac{1}{\overline{s}}\right), \ \overline{s} \to \infty, \tag{6.24}$$

$$\|q(x,\overline{s})\|_{C^{2+\gamma}(\overline{\Omega})} = O\left(\frac{1}{\overline{s}^2}\right), \ \overline{s} \to \infty. \tag{6.25}$$

6.4.2 The Sequence of Elliptic Equations

Considering the partition of the interval $[\underline{s}, \overline{s}]$ into N small subintervals of the length h,

$$\underline{s} = s_N < s_{N-1} < \ldots < s_0 = \overline{s}, \ s_{i-1} - s_i = h,$$

assuming that the function $q(x,s)$ is constant with respect to s in each of these subintervals, $q(x,s) := q_n(x)$, $s \in (s_n, s_{n-1}]$ and using the s-dependent CWF (2.38), we obtain similarly with Sect. 2.5 and 2.6.1 the following sequence of elliptic equations, which is similar with (2.49):

$$\Delta q_{n,k} - A_{1,n}\left(\chi_2(x)\, h \sum_{j=0}^{n-1} \nabla q_j - \nabla V_{n,k}\right) \nabla q_{n,k}$$

$$= -A_{2,n} h^2 \left(\sum_{j=0}^{n-1} \nabla q_j\right)^2 \chi_2(x) + 2A_{2,n} \nabla V_{n,k} \left(h \sum_{j=0}^{n-1} \nabla q_j\right) \chi_2(x)$$

$$-A_{2,n} (\nabla V_{n,k})^2, x \in \Omega, (n,k) \in [1,N] \times [1,m]. \tag{6.26}$$

Here,

$$q_0 := \equiv 0. \tag{6.27}$$

In (6.26), m is the number of iterations with respect to tails. We fix this number in the algorithm of this section. Boundary conditions for functions $q_{n,k}$ are

$$q_{n,k}|_{\Gamma_1} = \psi_{0,n}(x),\ \partial_{x_3} q_{n,k}|_{\Gamma_1} = \psi_{1,n}(x),\ \partial_n q_{n,k}|_{\Gamma_2 \cup \Gamma_3} = \frac{1}{s_n s_{n-1}}. \tag{6.28}$$

The third boundary condition (6.28) is obtained as follows. One can derive from (6.17) that

$$\partial_n q\,(x,s)\,|_{\Gamma_2 \cup \Gamma_3} = \frac{1}{s^2}. \tag{6.29}$$

Next, averaging over the interval (s_n, s_{n-1}) gives

$$\partial_n q_n|_{\Gamma_2 \cup \Gamma_3} = \frac{1}{h} \int\limits_{s_n}^{s_{n-1}} \frac{\mathrm{d}s}{s^2} = \frac{1}{s_n s_{n-1}}.$$

We assign then

$$\partial_n q_n|_{\Gamma_2 \cup \Gamma_3} := \frac{1}{s_n s_{n-1}}.$$

Functions $\psi_{0,n}(x)$ and $\psi_{1,n}(x)$ in (6.28) are obtained as follows. Let $\overline{g}_0(x,s)$ and $\overline{g}_1(x,s)$ be Laplace transforms (6.11) of functions $g_0(x,t)$ and $g_1(x,t)$, respectively. Then

$$w\,(x,s)\,|_{\Gamma_1} = \overline{g}_0\,(x,s)\,,\ \partial_n w\,(x,s)\,|_{\Gamma_1} = \overline{g}_1\,(x,s)\,.$$

Hence,

$$q\,(x,s)\,|_{\Gamma_1} = \frac{\partial}{\partial s}\left(\frac{\ln \overline{g}_0\,(x,s)}{s^2}\right) := \psi_0\,(x,s)\,, \tag{6.30}$$

$$\partial_n q\,(x,s)\,|_{\Gamma_1} = \frac{\partial}{\partial s}\left(\frac{\overline{g}_1\,(x,s)}{s^2 \overline{g}_0\,(x,s)}\right) = \psi_1\,(x,s)\,. \tag{6.31}$$

Thus, we set

$$\psi_{0,n}(x) = \frac{1}{h} \int\limits_{s_n}^{s_{n-1}} \psi_0\,(x,s)\,\mathrm{d}s,\ \psi_{1,n}(x) = \frac{1}{h} \int\limits_{s_n}^{s_{n-1}} \psi_1\,(x,s)\,\mathrm{d}s,\ x \in \Gamma_1.$$

In (6.26), $A_{1,n}, A_{2,n}$ are the same numbers as ones in Sect. 2.6.1.

There are three differences between (6.26) and (2.49). First, the nonlinear term $2\,(\nabla q_{n,k-1})^2\,(I_{1n}/I_0)$ is not present in (6.26), unlike (2.49). This is because this term is negligible for the case when in (2.38) $\lambda h \gg 1$; see (2.40). We have indeed discovered in our numerical studies that this term provides a very small impact in solutions of CIPs. We point out, however, that neglecting this term does not mean a linearization. Indeed, the nonlinear nature of the problem still surfaces in

terms containing ∇q_j as well as in gradients of tails $\nabla V_{n,k}$ in (6.26). Tails depend nonlinearly from functions $c_{n,k}$. The second difference between (6.26) and (2.49) is in the presence of the function $\chi_2(x)$ in (6.26), unlike (2.49). We need this presence for our convergence analysis. Finally, the third difference is in the absence of the term $-\varepsilon q_{n,k}$ in the left-hand side of (6.26), unlike (2.49).

6.4.3 The Iterative Process

First, we choose an initial tail function $V_{1,1}(x) \in C^{2+\gamma}\left(\overline{\Omega}\right)$. This can be either $V_{1,1}(x) \equiv 0$ or the function which corresponds to the solution of the problem (6.12), (6.13) for the case $c(x) \equiv 1$, which corresponds to the value of the function $c(x)$ outside the domain of interest Ω; see (6.3), or the choice described in Sect. 6.6.2; see (6.99), (6.100), and (6.101). These choice in our numerical studies are specified in Tests 1 and 2 of Sect. 6.8.4. Let $m \geq 1$ be an integer which we choose in numerical experiments. For each $n \in [1, N]$, we have m inner iterations with respect to the tails via computing functions $q_{n,k}, V_{n,k}, k \in [1, m]$.

Step n_k, where $n \in [1, N], k \in [1, m]$. Recall that by (6.27), $q_0 \equiv 0$. Suppose that functions $q_j \in H^5(\Omega), j \in [1, n-1]$ and tails $V_1, \ldots, V_{n-1}, V_{n,k} \in C^{2+\gamma}\left(\overline{\Omega}\right)$ are constructed. To construct the function $q_{n,k}$, we use the QRM described in Sect. 6.4.4. Hence, we obtain the function $q_{n,k} \in H^5(\Omega)$. To reconstruct an approximation $c_{n,k}(x)$ for the function $c(x)$, we first use the following discrete analogs of (6.22) and (6.23):

$$v_{n,k}(x, s_n) = -hq_{n,k}(x) - h\sum_{j=0}^{n-1} q_j(x) + V_{n,k}(x), x \in \Omega_{P_2}, \tag{6.32}$$

$$\overline{c}_{n,k}(x) = \Delta v_{n,k}(x, s_n) + s_n^2 \left|\nabla v_{n,k}(x, s_n)\right|^2, x \in \Omega_{P_2}. \tag{6.33}$$

Since we need (6.20), then, following (6.5), we set

$$c_{n,k}(x) = \begin{cases} \overline{c}_{n,k}(x), \text{ if } \overline{c}_{n,k}(x) \in [1, d], x \in \Omega_{P_2}, \\ 1, \text{ if } \overline{c}_{n,k}(x) < 1, x \in \Omega_{P_2}, \\ d, \text{ if } \overline{c}_{n,k}(x) > d, x \in \Omega_{P_2}. \end{cases} \tag{6.34}$$

Since functions $q_j, q_{n,k} \in H^5(\Omega)$, then the embedding theorem implies that $q_j, q_{n,k} \in C^3\left(\overline{\Omega}\right)$. In addition, the tail function $V_{n,k} \in C^{2+\gamma}\left(\overline{\Omega}\right)$. Hence, (6.32), (6.33), and (6.34) imply that

$$c_{n,k} \in C^{\gamma}\left(\overline{\Omega}_{P_2}\right). \tag{6.35}$$

Next, we construct the function $\widehat{c}_{n,k}(x)$ in (6.19). Hence, (6.34) and (6.35) imply (6.20).

Next, we solve the forward problem (6.12), (6.13) with $c(x) := \widehat{c}_{n,k}(x)$ for $s := \overline{s}$ and obtain the function $w_{n,k}(x,\overline{s})$. Both existence and uniqueness of the function $w_{n,k}(x,\overline{s})$ in the form (6.14), (6.15) are guaranteed by Theorem 2.7.2. We set for the new tail

$$V_{n,k+1}(x) = \frac{\ln w_{n,k}(x,\overline{s})}{\overline{s}^2} \in C^{2+\gamma}\left(\overline{\Omega}\right) \text{ if } k < m. \tag{6.36}$$

We also set

$$c_n(x) := c_{n,m}(x),\ q_n(x) := q_{n,m}(x),\ x \in \Omega, \tag{6.37}$$

$$V_n(x) := V_{n+1,1}(x) := V_{n,m+1}(x) := \tfrac{\ln w_{n,m}(x,\overline{s})}{\overline{s}^2},\ x \in \Omega. \tag{6.38}$$

6.4.4 The Quasi-Reversibility Method

Denote

$$a_{n,k}(x) = A_{1,n}\left(\chi_2(x)\, h \sum_{j=0}^{n-1} \nabla q_j - \nabla V_{n,k}\right), \tag{6.39}$$

$$H_{n,k}(x) = -A_{2,n}h^2\left(\sum_{j=0}^{n-1}\nabla q_j\right)^2 \chi_2(x) + 2A_{2,n}\nabla V_{n,k}\left(h\sum_{j=0}^{n-1}\nabla q_j\right)\chi_2(x)$$
$$-A_{2,n}\left(\nabla V_{n,k}\right)^2. \tag{6.40}$$

Note that the function $H_{n,k} \in L_2(\Omega)$. Because of (6.39), (6.40), the overdetermined boundary value problem (6.26), (6.28) can be rewritten as

$$\Delta q_{n,k} - a_{n,k}\nabla q_{n,k} = H_{n,k}, \tag{6.41}$$

$$q_{n,k}|_{\Gamma_1} = \psi_{0,n}(x),\ \partial_{x_3} q_{n,k}|_{\Gamma_1} = \psi_{1,n}(x),\ \partial_n q_{n,k}|_{\Gamma_2\cup\Gamma_3} = \tfrac{1}{s_n s_{n-1}}. \tag{6.42}$$

Since we have two boundary conditions rather then one at Γ_1, we find the "least squares" solution of the problem (6.41), (6.42) via the QRM. Specifically, we minimize the following Tikhonov functional

$$J^{\alpha}_{n,k}(u) = \frac{1}{2}\|\Delta u - a_{n,k}\nabla u - H_{n,k}\|^2_{L_2(\Omega)} + \frac{\alpha}{2}\|u\|^2_{H^5(\Omega)}, \tag{6.43}$$

subject to the boundary conditions (6.42). Here, $\alpha \in (0,1)$ is a small regularization parameter. Let $\overline{u}(x)$ be the unique minimizer of this functional, the existence of which is guaranteed by Lemma 6.5.2. Then we set $q_{n,k}(x) := \overline{u}(x)$. Local minima do not occur here since (6.43) is the sum of square norms of two expressions, both of which are linear with respect to u. The second term in the right-hand side of (6.43) is the Tikhonov regularization term. We use the $H^5(\Omega)$-norm here in order to ensure that the minimizer $u := q_{n,k} \in C^3\left(\overline{\Omega}\right)$. It was shown in Sect. 6.4.3 that the latter implies (6.35) and, therefore, (6.20). We call the minimizer $\overline{u}(x)$ of the functional $J^{\alpha}_{n,k}(u)$ *the QRM solution of the problem (6.41), (6.42).*

6.5 Estimates for the QRM

In this section, we temporary denote $x = (x,y,z)$. Although x denotes here both the vector and its first component, it will be always clear from the context what exactly x is in any particular place. It is convenient to scale variables in such a way that in (6.6)–(6.9) $P = 1/2$. Thus, in Sects. 6.5–6.7,

$$\Omega = \left\{x = (x,y,z) : (x,y) \in \left(-\frac{1}{4},\frac{1}{4}\right) \times \left(-\frac{1}{4},\frac{1}{4}\right),\ z \in \left(0,\frac{1}{2}\right)\right\}. \tag{6.44}$$

Below in Sects. 6.5–6.7, $C > 0$ denotes different generic constants which depend only on the domain Ω in (6.44), $(\cdot,\cdot)$ denotes the scalar product in $L_2(\Omega)$, and $[\cdot,\cdot]$ denotes the scalar product in $H^5(\Omega)$.

Let $\lambda, \nu > 2$ be two parameters. Introduce the z-dependent CWF $K(z)$:

$$K(z) := K_{\lambda,\nu}(z) = \exp(\lambda \rho^{-\nu}),\ \text{where } \rho(z) = z + \frac{1}{4},\ z > 0.$$

This CWF is different from the ones previously used for Carleman estimates for elliptic PDEs; see, for example, the function φ in (1.172) (Sect. 1.10.7) for the case when its dependence from t is dropped. Note that $\rho(z) \in (0,3/4)$ in Ω and $\rho(z)\mid_{\Gamma_3} = 3/4$. Let the number $\varkappa \in (1/3,1)$. Denote

$$\Omega_{\varkappa} = \left\{x \in \Omega : \rho(z) < \frac{3}{4}\varkappa\right\}.$$

Hence, if $\varkappa_1 < \varkappa_2$, then $\Omega_{\varkappa_1} \subset \Omega_{\varkappa_2}$. Also, $\Omega_1 = \Omega$ and $\Omega_{1/3} = \varnothing$. In addition,

$$K^2(z) \geq \exp\left[2\lambda\left(\frac{4}{3}\varkappa\right)^{\nu_0}\right] \text{ in } \Omega_{\varkappa}.$$

Lemma 6.5.1. *Fix the parameter $\nu > 2$. Consider an arbitrary function $u \in H^3(\Omega)$ such that*

$$u\mid_{\Gamma_1} = u_z\mid_{\Gamma_1} = \partial_n u\mid_{\Gamma_2} = 0. \tag{6.45}$$

Then there exists a constant $C > 0$ such that for all $\lambda > 2$ the following Carleman estimate is valid for all these functions u:

$$\int_\Omega (\Delta u)^2 K^2 \mathrm{d}x \geq \frac{C}{\lambda} \sum_{|\alpha|=2} \int_\Omega \left(D^\alpha u\right)^2 K^2 \mathrm{d}x + C \int_\Omega \left[\lambda \left(\nabla u\right)^2 + \lambda^3 u^2\right] K^2 \mathrm{d}x$$
$$-C\lambda^3 \|u\|^2_{H^3(\Omega)} \exp\left[2\lambda \left(\frac{4}{3}\right)^\nu\right].$$

Proof. We have

$$\begin{aligned}
\left(\Delta u\right)^2 K^2 &= \left(u_{xx}^2 + u_{yy}^2 + u_{zz}^2 + 2u_{xx}u_{zz} + 2u_{xx}u_{yy} + 2u_{yy}u_{zz}\right) K^2 \\
&= \left(u_{xx}^2 + u_{yy}^2 + u_{zz}^2\right) K^2 + \partial_x \left(2u_x u_{zz} K^2 + 2u_x u_{yy} K^2\right) \\
&\quad + \partial_y \left(2u_y u_{zz} K^2\right) - 2u_x u_{zzx} K^2 - 2u_x u_{yyx} K^2 - 2u_y u_{zzy} K^2 \\
&= \left(u_{xx}^2 + u_{yy}^2 + u_{zz}^2\right) K^2 + \partial_x \left(2u_x u_{zz} K^2 + 2u_x u_{yy} K^2\right) \\
&\quad + \partial_y \left(2u_y u_{zz} K^2\right) + \partial_y \left(-2u_x u_{xy} K^2\right) + 2u_{xy}^2 K^2 \\
&\quad + \partial_z \left(-2u_x u_{xz} K^2\right) + 2u_{xz}^2 K^2 - 4\lambda\nu\rho^{-\nu-1} u_x u_{xz} K^2 \\
&\quad + \partial_z \left(-2u_y u_{yz} K^2\right) + 2u_{yz}^2 K^2 - 4\lambda\nu\rho^{-\nu-1} u_y u_{yz} K^2.
\end{aligned}$$

Thus, we have obtained that

$$\begin{aligned}
\left(\Delta u\right)^2 K^2 &= \left(u_{xx}^2 + u_{yy}^2 + u_{zz}^2 + 2u_{xy}^2 + 2u_{xz}^2 + 2u_{yz}^2\right) K^2 \\
&\quad - 4\lambda\nu\rho^{-\nu-1} \left(u_x u_{xz} + u_y u_{yz}\right) K^2 + \partial_x \left[2\left(u_x u_{zz} + u_x u_{yy}\right) K^2\right] \\
&\quad + \partial_y \left[2\left(u_y u_{zz} - u_x u_{xy}\right) K^2\right] + \partial_z \left[-2\left(u_x u_{xz} + u_y u_{yz}\right) K^2\right].
\end{aligned} \tag{6.46}$$

Using the Cauchy–Schwarz inequality,

$$2ab \geq -\varepsilon a^2 - \frac{b^2}{\varepsilon},\ \forall \varepsilon > 0,$$

and taking $\varepsilon = 1/4$, we obtain

$$-4\lambda\nu\rho^{-\nu-1} \left(u_x u_{xz} + u_y u_{yz}\right) K^2 \geq -\left(u_{xz}^2 + u_{yz}^2\right) K^2 - 4\lambda^2\nu^2\rho^{-2\nu-2} \left(\nabla u\right)^2 K^2.$$

Hence, (6.46) implies that

$$(\Delta u)^2 K^2 \geq \sum_{|\alpha|=2} (D^\alpha u)^2 K^2 - 4\lambda^2 \nu^2 \rho^{-2\nu-2} (\nabla u)^2 K^2$$
$$+\partial_x \left[2u_x \left(u_{zz} + u_{yy}\right) K^2\right] + \partial_y \left[2 \left(u_y u_{zz} - u_x u_{xy}\right) K^2\right]$$
$$+\partial_z \left[-2 \left(u_x u_{xz} + u_y u_{yz}\right) K^2\right]. \tag{6.47}$$

Consider a new function $v = uK$. Substituting $u = vK^{-1}$, we obtain

$$(\Delta u)^2 \rho^{\nu+1} K^2 = (y_1 + y_2 + y_3)^2 \rho^{\nu+1} \geq 2y_2(y_1 + y_3)\rho^{\nu+1}, \tag{6.48}$$

$$y_1 = \Delta v,\ y_2 = 2\lambda\nu\rho^{-\nu-1} v_z,\ y_3 = (\lambda\nu)^2 \rho^{-2\nu-2}(1 - (\nu+1)(\lambda\nu)^{-1}\rho^\nu)v. \tag{6.49}$$

We have

$$2y_1 y_2 \rho^{\nu+1} = \partial_x \left(4\lambda\nu v_z v_x\right) + \partial_y \left(4\lambda\nu v_z v_y\right) + \partial_z \left[2\lambda\nu \left(v_z^2 - v_x^2 - v_y^2\right)\right]. \tag{6.50}$$

Next, by (6.48) and (6.49),

$$2y_2 y_3 \rho^{\nu+1} = 4(\lambda\nu)^3 \left(\rho^{-2\nu-2} - (\nu+1)(\lambda\nu)^{-1}\rho^{-\nu-2}\right) v_z v$$
$$= \partial_z \left[2(\lambda\nu)^3 \left(\rho^{-2\nu-2} - (\nu+1)(\lambda\nu)^{-1}\rho^{-\nu-2}\right) v^2\right]$$
$$+4(\lambda\nu)^3 (\nu+1)\rho^{-2\nu-3} \left(1 - (\nu+2)(2\lambda\nu)^{-1}\rho^\nu\right) v^2$$
$$\geq 2\lambda^3 \nu^4 \rho^{-2\nu-3} v^2 + \partial_z \left[2(\lambda\nu)^3 \left(\rho^{-2\nu-2} - (\nu+1)(\lambda\nu)^{-1}\rho^{-\nu-2}\right) v^2\right].$$

Hence,

$$2y_2 y_3 \rho^{\nu+1} \geq 2\lambda^3 \nu^4 \rho^{-2\nu-3} v^2 + \partial_z \left[2(\lambda\nu)^3 \left(\rho^{-2\nu-2} - (\nu+1)(\lambda\nu)^{-1}\rho^{-\nu-2}\right) v^2\right]. \tag{6.51}$$

Summing up (6.50) with (6.51), using (6.48) and the backward substitution $u = vK$, we obtain

$$(\Delta u)^2 \rho^{\nu+1} K^2 \geq 2\lambda^3 \nu^4 \rho^{-2\nu-3} u^2 K^2 + \partial_x U_1 + \partial_y U_2 + \partial_z U_3, \tag{6.52}$$

where the following estimates are valid for functions U_1, U_2, U_3:

$$\begin{aligned} |U_1| &\leq C\lambda\nu\left|u_x\right|\left(\left|u_z\right|+\lambda\nu\rho^{-\nu-1}\left|u\right|\right)K^2, \\ |U_2| &\leq C\lambda\nu\left|u_y\right|\left(\left|u_z\right|+\lambda\nu\rho^{-\nu-1}\left|u\right|\right)K^2, \\ |U_3| &\leq C\lambda\nu\left(|\nabla u|^2+\lambda^2\nu^2\rho^{-2\nu-2}u^2\right)K^2. \end{aligned} \tag{6.53}$$

We now need to incorporate the term $\lambda\left(\nabla u\right)^2 K^2$ in the right-hand side of the Carleman estimate. Hence, we continue as follows:

$$\begin{aligned} -\lambda\nu u\Delta uK^2 &= \partial_x\left(-\lambda\nu uu_xK^2\right)+\partial_y\left(-\lambda\nu uu_yK^2\right)+\partial_z\left(-\lambda\nu uu_zK^2\right) \\ &\quad +\lambda\nu\left(\nabla u\right)^2K^2-2\lambda^2\nu^2\rho^{-\nu-1}u_zuK^2 \\ &= \lambda\nu\left(\nabla u\right)^2K^2-2\lambda^3\nu^3\rho^{-2\nu-2}\left(1+\left(\nu+1\right)\left(2\lambda\nu\right)^{-1}\rho^{\nu}\right)u^2K^2 \\ &\quad +\partial_xU_4+\partial_yU_5+\partial_zU_6. \end{aligned}$$

Hence,

$$-\lambda\nu u\Delta uK^2 \geq \lambda\nu\left(\nabla u\right)^2K^2-4\lambda^3\nu^3\rho^{-2\nu-2}u^2K^2+\partial_xU_4+\partial_yU_5+\partial_zU_6, \tag{6.54}$$

$$U_4=-\lambda\nu uu_xK^2,\ U_5=-\lambda\nu uu_yK^2, |U_6|\leq C\left(\lambda\nu u_z^2+\lambda^2\nu^2\rho^{-\nu-1}u^2\right)K^2. \tag{6.55}$$

Summing up (6.52) and (6.54) and taking into account (6.53) and (6.55) as well as the fact that

$$2\lambda^3\nu^4\rho^{-2\nu-3}-4\lambda^3\nu^3\rho^{-2\nu-2}=2\lambda^3\nu^4\rho^{-2\nu-3}\left(1-\rho\left(2\nu\right)^{-1}\right)>\lambda^3\nu^4\rho^{-2\nu-3},$$

we obtain

$$\begin{aligned} &(\Delta u)^2K^2-\lambda\nu u\Delta uK^2\geq\lambda\nu\left(\nabla u\right)^2K^2+\lambda^3\nu^4\rho^{-2\nu-3}u^2K^2 \\ &+\partial_xU_7+\partial_yU_8+\partial_zU_9, \end{aligned} \tag{6.56}$$

$$|U_7|\leq C\lambda\nu\left|u_x\right|\left(\left|u_z\right|+\lambda\nu\rho^{-\nu-1}\left|u\right|\right)K^2, \tag{6.57}$$

$$|U_8|\leq C\lambda\nu\left|u_y\right|\left(\left|u_z\right|+\lambda\nu\rho^{-\nu-1}\left|u\right|\right)K^2, \tag{6.58}$$

$$|U_9|\leq C\lambda\nu\left(|\nabla u|^2+\lambda^2\nu^2\rho^{-2\nu-2}u^2\right)K^2. \tag{6.59}$$

Since the number $\nu \geq 2$ is fixed, we can incorporate ν in C. Also, since $\rho^{\nu+1} < 1$, we can regard that $\rho^{\nu+1} < C$. By the Cauchy–Schwarz inequality,

$$-\lambda \nu u \Delta u K^2 \leq \frac{1}{2}(\Delta u)^2 \rho^{\nu+1} K^2 + \frac{1}{2}\lambda^2 \nu^2 \rho^{-\nu-1} u^2 K^2.$$

Hence, we obtain from (6.56), (6.57), (6.58), and (6.59)

$$(\Delta u)^2 K^2 \geq C\left[\lambda (\nabla u)^2 + \lambda^3 u^2\right] K^2 + \partial_x U_7 + \partial_y U_8 + \partial_z U_9. \tag{6.60}$$

We now divide (6.47) by λr with a constant $r = r(\nu) > 0$ such that $4\nu_0^2 \rho^{-2\nu_0-2}/r \leq C/2$, add the resulting inequality to (6.60), and take into account (6.57), (6.58), and (6.59). Then with a new constant C, we obtain the following pointwise Carleman estimate for the Laplace operator in the domain Ω:

$$(\Delta u)^2 K^2 \geq \frac{C}{\lambda} \sum_{|\alpha|=2} \left(D^\alpha u\right)^2 K^2 + C\left[\lambda (\nabla u)^2 + \lambda^3 u^2\right] K^2$$
$$+\partial_x U_{10} + \partial_y U_{11} + \partial_z U_{12}, \tag{6.61}$$

$$|U_{10}| \leq C\lambda |u_x| \left(|u_{zz}| + |u_{yy}| + |u_z| + \lambda |u|\right) K^2, \tag{6.62}$$

$$|U_{11}| \leq C\left[\lambda |u_y| \left(|u_{zz}| + |u_z| + \lambda |u|\right) + |u_{xy}| |u_x|\right] K^2, \tag{6.63}$$

$$|U_{12}| \leq C\lambda\left[|u_{xz}|^2 + |u_{yz}|^2 + |\nabla u|^2 + \lambda^2 u^2\right] K^2. \tag{6.64}$$

We now integrate both sides of formula (6.61) over the rectangle Ω using the Gauss' formula. It is *important* that because of (6.45) and estimates (6.62)–(6.64), each resulting boundary integral over Γ_1 and Γ_2 will turn out to be zero. We obtain

$$\int_\Omega (\Delta u)^2 K^2 \mathrm{d}x \geq \frac{C}{\lambda} \sum_{|\alpha|=2} \int_\Omega \left(D^\alpha u\right)^2 K^2 \mathrm{d}x + C \int_\Omega \left[\lambda (\nabla u)^2 + \lambda^3 u^2\right] K^2 \mathrm{d}x$$
$$-C\lambda \int_{\Gamma_3} \left[|u_{xz}|^2 + |u_{yz}|^2 + |\nabla u|^2 + \lambda^2 u^2\right] K^2 \mathrm{d}S. \tag{6.65}$$

Note that

$$K^2\left(\frac{1}{2}\right) = K^2(z)|_{\Gamma_3} = \min_{\overline{\Omega}} K^2(z) = \exp\left[2\lambda\left(\frac{4}{3}\right)^\nu\right].$$

Hence,

$$\int_{\Gamma_3} \lambda\left[|u_{xz}|^2 + |u_{yz}|^2 + |\nabla u|^2 + \lambda^2 u^2\right] K^2 \mathrm{d}x \leq C\lambda^3 \|u\|^2_{H^3(\Omega)} \exp\left[2\lambda\left(\frac{4}{3}\right)^\nu\right].$$

Substituting this in (6.65), we obtain the estimate of this lemma. □

We now establish both existence and uniqueness of the minimizer of the functional (6.43). Denote $a_{n,k}^{(i)}(x), i = 1,2,3$ components of the vector function $a_{n,k}(x)$ in (6.39). Let

$$\left\| a_{n,k}^{(i)} \right\|_{L_\infty(\Omega)} \leq M,\ M = \text{const.} > 0, i = 1,2,3. \tag{6.66}$$

Lemma 6.5.2. *Assume that there exists a function $\Phi \in H^5(\Omega)$ satisfying boundary conditions (6.42). Also, assume that condition (6.66) holds. Then there exists unique minimizer $u \in H^5(\Omega)$ of the functional (6.43). Furthermore, with a constant $C_1 = C_1(M) > 0$,*

$$\|u\|_{H^5(\Omega)} \leq \frac{C_1}{\sqrt{\alpha}} \left(\|H_{n,k}\|_{L_2(\Omega)} + \|\Phi\|_{H^5(\Omega)} \right).$$

Proof. Let $U = u - \Phi$. Then the function U satisfies boundary conditions (6.45). By the variational principle,

$$(G_{n,k}U, G_{n,k}v) + \alpha [U,v] = (H_{n,k} - G_{n,k}\Phi, G_{n,k}v) - \alpha [\Phi, v],$$

for all functions $v \in H^5(\Omega)$ satisfying boundary conditions (6.45). Here,

$$G_{n,k}U := \Delta U - a_{n,k}\nabla U. \tag{6.67}$$

The rest of the proof follows from the Riesz theorem. □

Lemma 6.5.3. *Let $G_{n,k}$ be the operator defined in (6.67). Let the function $u \in H^5(\Omega)$ satisfy boundary conditions (6.45) as well as the variational equality*

$$(G_{n,k}u, G_{n,k}v) + \alpha [u,v] = (H_{n,k}, G_{n,k}v) + \alpha [g,v] \tag{6.68}$$

for all functions $v \in H^5(\Omega)$ satisfying (6.45). Then

$$\|u\|_{H^5(\Omega)} \leq \frac{1}{\sqrt{\alpha}} \|H_{n,k}\|_{L_2(\Omega)} + \|g\|_{H^5(\Omega)}.$$

Proof. Set in (6.68) $v := u$ and use the Cauchy–Schwarz inequality. □

Theorem 6.5. *Let $G_{n,k}$ be the operator defined in (6.67). Assume that condition (6.66) holds. Let $g \in H^5(\Omega)$ be an arbitrary function. Let $u \in H^5(\Omega)$ be the function satisfying boundary conditions (6.45) as well as the variational equality (6.68) for all functions $v \in H^5(\Omega)$ satisfying (6.45). Let the number $\varkappa \in (1/3, 1)$ and the number $\beta \in (\varkappa, 1)$. Consider the numbers b_1, b_2,*

$$b_1 := b_1(\beta) = \frac{1}{2\left[1+(1-\beta^{\nu})(3\beta)^{-\nu}\right]} \in \left(0, \frac{1}{2}\right), \tag{6.69}$$

$$b_2 := b_2(\beta) = \frac{1}{2} - b_1 > 0, \tag{6.70}$$

where ν is the parameter of Lemma 6.5.1. Then there exists a sufficiently small number $\alpha_1 = \alpha_1(M,\beta) \in (0,1)$ such that for all $\alpha \in (0,\alpha_1)$ the following estimate holds with a constant $C_2 = C_2(M,\Omega) > 0$

$$\|u\|_{H^2(\Omega_x)} \leq C_2 \alpha^{-b_1} \|H_{n,k}\|_{L_2(\Omega)} + C_2 \alpha^{b_2} \|g\|_{H^5(\Omega)}. \tag{6.71}$$

Proof. In this proof, $C_2 = C_2(M,\Omega)$ denotes different constants depending only from M and Ω. Setting in (6.68) $v := u$ and using the Cauchy–Schwarz inequality, we obtain

$$\|G_{n,k}u\|^2_{L_2(\Omega)} \leq F^2 := \|H_{n,k}\|^2_{L_2(\Omega)} + \alpha \|g\|^2_{H^5(\Omega)}. \tag{6.72}$$

Note that

$$K^2(0) = \max_{\overline{\Omega}} K^2(z) = \exp(2\lambda \cdot 4^{\nu}).$$

Hence, we obtain from (6.72)

$$F^2 \geq \|G_{n,k}u\|^2_{L_2(\Omega)} = \left\|K^{-1}K \cdot G_{n,k}u\right\|^2_{L_2(\Omega)} \geq \frac{1}{K^2(0)} \|K \cdot G_{n,k}u\|^2_{L_2(\Omega)}$$
$$= \exp(-2\lambda \cdot 4^{\nu}) \|K \cdot G_{n,k}u\|^2_{L_2(\Omega)}.$$

Clearly

$$(G_{n,k}u)^2 K^2 \geq \frac{1}{2}(\Delta u)^2 K^2 - C_1 (\nabla u)^2 K^2.$$

Hence,

$$\int_{\Omega} (\Delta u)^2 K^2 \mathrm{d}x\mathrm{d}z \leq C_1 \int_{\Omega} (\nabla u)^2 K^2 \mathrm{d}x\mathrm{d}z + \exp(2\lambda \cdot 4^{\nu}) F^2. \tag{6.73}$$

Applying Lemma 6.5.1 to (6.73), choosing $\lambda > 1$ sufficiently large, and observing that the term with $(\nabla u)^2$ in (5.14) will be absorbed for such λ, we obtain

$$\lambda \exp(2\lambda \cdot 4^{\nu}) F^2 + C_2 \lambda^4 \|u\|^2_{H^3(\Omega)} \exp\left[2\lambda \left(\frac{4}{3}\right)^{\nu}\right]$$
$$\geq C_2 \sum_{|\alpha| \leq 2} \int_{\Omega} (D^{\alpha}u)^2 K^2 \mathrm{d}x$$

$$\geq C_2 \sum_{|\alpha|\leq 2} \int_{\Omega_\varkappa} (D^\alpha u)^2 \, K^2 \mathrm{d}x$$

$$\geq C_2 \exp\left[2\lambda \left(\frac{4}{3\varkappa}\right)^\nu\right] \|u\|^2_{H^2(\Omega)}.$$

Recalling that $\beta \in (\varkappa, 1)$, we obtain that the latter sequence of inequalities implies that

$$\lambda \exp\left(2\lambda \cdot 4^\nu\right) F^2 + C_2 \lambda^4 \|u\|^2_{H^3(\Omega)} \exp\left[2\lambda \left(\frac{4}{3}\right)^\nu\right]$$

$$\geq C_1 \exp\left[2\lambda \left(\frac{4}{3\varkappa}\right)^\nu\right] \|u\|^2_{H^2(\Omega)} \geq C_2 \exp\left[2\lambda \left(\frac{4}{3\beta}\right)^\nu\right] \|u\|^2_{H^2(\Omega)}.$$

Thus,

$$\lambda \exp\left(2\lambda \cdot 4^\nu\right) F^2 + C_2 \lambda^4 \|u\|^2_{H^3(\Omega)} \exp\left[2\lambda \left(\frac{4}{3}\right)^\nu\right]$$

$$\geq C_2 \exp\left[2\lambda \left(\frac{4}{3\beta}\right)^\nu\right] \|u\|^2_{H^2(\Omega)}.$$

Dividing this inequality by the exponential term in the right-hand side, we obtain a stronger estimate:

$$\|u\|^2_{H^2(\Omega_\varkappa)} \leq C_2 \exp\left(2\lambda \cdot 4^\nu\right) F^2 + C_2 \|u\|^2_{H^3(\Omega)} \exp\left[-2\lambda \left(\frac{4}{3\beta}\right)^\nu (1-\beta^\nu)\right]. \tag{6.74}$$

Applying Lemma 6.5.3 to $\|u\|^2_{H^3(\Omega)}$ in the right-hand side of (6.74), we obtain

$$\|u\|^2_{H^2(\Omega_\varkappa)} \leq C_2 F^2 \left\{\exp\left(2\lambda \cdot 4^\nu\right) + \frac{1}{\alpha} \exp\left[-2\lambda \left(\frac{4}{3\beta}\right)^\nu (1-\beta^\nu)\right]\right\}. \tag{6.75}$$

Since $\alpha \in (0, \alpha_0)$ and α_0 is sufficiently small, we can choose sufficiently large $\lambda = \lambda(\alpha)$ such that

$$\exp\left(2\lambda \cdot 4^\nu\right) = \alpha^{-1} \exp\left[-2\lambda \left(\frac{4}{3\beta}\right)^\nu (1-\beta^\nu)\right]. \tag{6.76}$$

We obtain from (6.76) that $2\lambda \cdot 4^\nu = \ln \alpha^{-2b_1}$. Hence, (6.74), (6.75), and (6.76) imply the validity of (6.71). □

6.6 The Third Approximate Mathematical Model

6.6.1 Exact Solution

First, we need to introduce the definition of the exact solution. Some aspects of this definition are different from the definition of Sect. 2.8.1. We assume that there exists a coefficient $c^*(x)$ which is the unique exact solution of coefficient inverse problem 6.2 with the exact data $g_0^*(x,t)$, $g_1^*(x,t)$ in (6.10). We assume that

$$c^* \in \mathbb{M} \cap C^4\left(\mathbb{R}^3\right), \tag{6.77}$$

where $\mathbb{M}$ was defined in (6.5). The assumption (6.77) is because of (6.3) and (6.4). Let $u^*(x,t)$ be the solution of the forward problem (6.1), (6.2) with $c := c^*$ and $w^*(x,s)$ be its Laplace transform (3.3) for $s > \underline{s} = \underline{s}(c^*) > 0$ (Theorem 2.7.1 Since the source $x_0 \notin \overline{\Omega}$, then it follows from (6.77) and Theorem 2.7.2 that $w^*(x,s) \in C^{5+\gamma}\left(\overline{\Omega}\right)$. Similarly with (6.21), let

$$v^*(x,s) = \frac{\ln w^*(x,s)}{s^2},\ q^*(x,s) = \frac{\partial v^*(x,s)}{\partial s}. \tag{6.78}$$

Let $[\underline{s}, \overline{s}]$ be the s-interval of Sect. 6.4 and $\underline{s} > \underline{s}(c^*)$. Since $w^*(x,s) \in C^{5+\gamma}\left(\overline{\Omega}\right)$, we assume that

$$q^* \in C^{5+\gamma}\left(\overline{\Omega}\right) \times C^1[\underline{s}, \overline{s}], \tag{6.79}$$

$$\|q^*(x,s)\|_{C^{5+\gamma}(\overline{\Omega}) \times C^1[\underline{s},\overline{s}]} \leq C^*, \tag{6.80}$$

$$C^* = \text{const.} \geq 2, \tag{6.81}$$

where the constant C^* is given. Consider the same partition of the interval $[\underline{s}, \overline{s}]$ into N small subintervals as one in Sect. 6.4.2. Let $q_n^*(x)$ be the average of the function $q^*(x,s)$ over the interval (s_n, s_{n-1}):

$$q_n^*(x) = \frac{1}{h} \int_{s_n}^{s_{n-1}} q^*(x,s)\, \mathrm{d}s.$$

Then (6.79) and (6.80) imply that

$$\max_{s \in [s_n, s_{n-1}]} \|q_n^*(x) - q^*(x,s)\|_{C^{5+\gamma}(\overline{\Omega})} \leq C^* h. \tag{6.82}$$

Hence, increasing, if necessary, the number C^*, we can assume that

$$\max_{1 \leq n \leq N} \|q_n^*\|_{H^5(\Omega)} \leq C^*. \tag{6.83}$$

Let

$$\psi_0^*(x,s) := q^*(x,s)\mid_{\Gamma_1},\ \psi_1^*(x,s) := \partial_{x_3} q^*(x,s)\mid_{\Gamma_1},\ s \in [\underline{s},\overline{s}]. \tag{6.84}$$

Given (6.84), let functions $\psi_{0,n}^*(x)$ and $\psi_{1,n}^*(x)$ be averages of functions $\psi_0^*(x,s)$ and $\psi_1^*(x,s)$ over the interval (s_n, s_{n-1}). Then boundary conditions for functions $q_n^*(x)$ at Γ_1 are

$$q_n^*|_{\Gamma_1} = \psi_{0,n}^*(x), \partial_{x_3} q_n^*|_{\Gamma_1} = \psi_{1,n}^*(x). \tag{6.85}$$

The exact tail function $V^*(x)$ is

$$V^*(x) = \frac{\ln w^*(x,\overline{s})}{\overline{s}^2}. \tag{6.86}$$

The function q_n^* satisfies the following analogue of (6.26):

$$\begin{aligned}
&\Delta q_n^* - A_{1,n}\left(h\sum_{j=0}^{n-1}\nabla q_j^*(x) - \nabla V^*\right)\nabla q_n^* \\
&= -A_{2,n}h^2\left(\sum_{j=0}^{n-1}\nabla q_j^*(x)\right)^2 + 2A_{2,n}\nabla V^*\left(h\sum_{j=0}^{n-1}\nabla q_j^*(x)\right) \\
&\quad -A_{2,n}\left(\nabla V^*\right)^2 + F_{1,n}(x,h,\lambda), \quad q_0^* :\equiv 0.
\end{aligned} \tag{6.87}$$

Similarly with (6.32) and (6.33),

$$v_n^*(x) := -hq_n^*(x) - h\sum_{j=0}^{n-1} q_j^*(x) + V^*(x) + F_{2,n}(x,h), x \in \Omega, \tag{6.88}$$

$$c^*(x) = \Delta v_n^*(x) + s_n^2\left|\nabla v_n^*(x)\right|^2 + F_{3,n}(x,h), x \in \Omega. \tag{6.89}$$

In (6.87)–(6.89) functions $F_{1,n}(x,h,\lambda)$, $F_{2,n}(x,h)$, $F_{3,n}(x,h)$ represent approximation errors. In particular, the nonlinear term $2(I_{1n}/I_0)\left(\nabla q_n^*\right)^2$, an analog of which was ignored in (6.26), is a part of $F_{1,n}$. Although we can prove an analog of Theorem 6.7 for the case

$$F_{1,n} \neq 0, F_{2,n} \neq 0, F_{3,n} \neq 0, \psi_{0,n}^* \neq \psi_{0,n}, \psi_{1,n}^* \neq \psi_{1,n},$$

this would require more space while the method of the proof would be almost the same. Hence, we "allow" now the error in the boundary data at Γ_1 to be present only at $s := \bar{s}$, see Lemma 6.7. Therefore, for *brevity only* we assume below that

$$F_{1,n} = F_{2,n} = F_{2,3} = 0, \psi_{0,n}^* = \psi_{0,n}, \psi_{1,n}^* = \psi_{1,n},\ n \in [1,N]. \tag{6.90}$$

Using, the idea of the proof of Theorem 2.7.2, it is possible to prove that not only the function $w^*(x,s) \in C^{5+\gamma}(\overline{\Omega})$ but also the functions $D_s^k w^*(x,s) \in C^{5+\gamma}(\overline{\Omega}), k = 1,2$. Since this implies that $q^*(x,s) \in C^{5+\gamma}(\overline{\Omega}) \times C^1[\underline{s},\overline{s}]$, then it is not necessary to impose this assumption in (6.79). However, we still prefer to use this assumption because the proof of (6.79) is not our main focus. The reason why we require the C^4-smoothness of c^* in (6.4) and (6.77) is to ensure that $V^* \in C^{5+\gamma}(\overline{\Omega})$. We need the latter to justify that the function $p^* \in H^5(\Omega)$ in (6.92).

6.6.2 The Third Approximate Mathematical Model

The third approximate mathematical model is similar with the second one of Sect. 2.9.2 Some differences with Sect. 2.9.2 are due to the fact that we use the backscattering data now, which was not the case of Sect. 2.9.2. Similarly with Sect. 2.9.2, Assumptions 1–3 below mean that we take into account only the first term of the asymptotic behavior of the function $s^{-2}\ln w^*(x,s)$ at $s \to \infty$ and ignore the rest. By (2.105) (Sect. 2.8.1), the equation for the function q^* is

$$\Delta q^* - 2s^2\nabla q^* \int_s^{\overline{s}} \nabla q^*(x,\tau)\,d\tau + 2s\left[\int_s^{\overline{s}} \nabla q^*(x,\tau)\,d\tau\right]^2 + 2s^2\nabla q^*\nabla V^*$$
$$- 2s\nabla V^* \int_s^{\overline{s}} \nabla q^*(x,\tau)\,d\tau + 2s\left(\nabla V^*\right)^2 = 0, \quad (x,s) \in \Omega \times [\underline{s},\overline{s}]. \tag{6.91}$$

The third approximate mathematical model consists of the following three **assumptions:**

1. There exists a function $p^*(x) \in H^5(\Omega)$ such that the exact tail function $V^*(x)$ has the form
$$V^*(x,s) = \frac{p^*(x)}{s}, \ \forall s \geq \overline{s}. \tag{6.92}$$
And also (see (6.86)),
$$\frac{p^*(x)}{\overline{s}} = \frac{\ln w^*(x,\overline{s})}{\overline{s}^2}. \tag{6.93}$$
2. There exists unique exact solution c^* of CIP 6.2 satisfying condition (6.77). For $\overline{s} > \underline{s} > \underline{s}(c^*) > 0$, the function $q^*(x,s), (x,s) \in \Omega \times [\underline{s},\overline{s}]$ defined in (6.78), satisfies conditions (6.79), (6.80).
3. For $s \in [\underline{s},\overline{s}]$, the function $q^*(x,s)$ satisfies boundary conditions (6.84) at Γ_1 as well as the boundary condition (6.29) at $\Gamma_2 \cup \Gamma_3$:

$$\partial_n q(x,s)\mid_{\Gamma_2\cup\Gamma_3} = \frac{1}{s^2}. \tag{6.94}$$

Since $q^*(x,s) = \partial_s V^*(x,s)$ for $s \geq \overline{s}$, we derive from (6.92) that

$$q^*(x,\overline{s}) = -\frac{p^*(x)}{\overline{s}^2}. \tag{6.95}$$

Recall that the boundary condition (6.29) is an approximate one and this is why we treat (6.94) as an assumption. It follows from (6.94) that

$$\partial_n q_n^*\mid_{\Gamma_2\cup\Gamma_3} = \frac{1}{s_n s_{n-1}}. \tag{6.96}$$

Set in (6.91) $s = \overline{s}$. Then, using (6.84) and (6.92), (6.95) and (6.94), we obtain the following *approximate* PDE and boundary conditions for the function $p^*(x)$:

$$\Delta p^* = 0 \text{ in } \Omega,\ p^* \in H^5(\Omega), \tag{6.97}$$

$$p^*|_{\Gamma_1} = -\overline{s}^2\psi_0^*(x,\overline{s}),\ \partial_n p^*|_{\Gamma_1} = -\overline{s}^2\psi_1^*(x,\overline{s}),\ \partial_n p^*\mid_{\Gamma_2\cup\Gamma_3} = -1. \tag{6.98}$$

The existence of the solution of the problem (6.97), (6.98) is assumed rather than proved because conditions (6.97) and (6.98) are derived from assumptions 1–3, and (6.94) is an approximate boundary condition. Let functions $\psi_0(x,s), \psi_1(x,s)$ be boundary conditions in (6.30), (6.31) (Sect. 6.4.2). Suppose that for each $\alpha \in (0,1)$, there exists the QRM solution $p = p(x;\alpha)$ of the following boundary value problem:

$$\Delta p = 0 \text{ in } \Omega,\ p(x) \in H^5(\Omega), \tag{6.99}$$

$$p|_{\Gamma_1} = -\overline{s}^2\psi_0(x,\overline{s}),\ \partial_n p|_{\Gamma_1} = -\overline{s}^2\psi_1(x,\overline{s}),\ \partial_n p\mid_{\Gamma_2\cup\Gamma_3} = -1; \tag{6.100}$$

see Lemma 6.7 for the existence and uniqueness of the function p. Then, we choose an appropriate $\alpha \in (0,1)$. Next, we set the first approximation for the tail function in the iterative process of Sect. 6.4.3 as (also, see Remarks 2.9.2)

$$V_{1,1}(x) := V_{1,1}(x;\alpha) := \frac{p(x;\alpha)}{\overline{s}}. \tag{6.101}$$

Remark 6.6.2. Analogs of Remarks 2.9.2 are valid here.

We now establish uniqueness within the framework of the third approximate mathematical model. Although uniqueness can be proven under less restrictive assumptions imposed on functions q^*, p^* than ones above, we are not doing this here for brevity.

Lemma 6.6.2. *Suppose that above Assumptions 1–3 hold. Then for* $(x,s) \in \Omega \times [\underline{s},\overline{s}]$, *there exists at most one function* $q^*(x,s)$ *satisfying conditions (6.79), (6.80) as well as (6.91). In addition, if assuming the continuous analog of (6.89),*

$$c^*(x) = \Delta v^*(x) + s^2 |\nabla v^*(x)|^2, (x,s) \in \Omega \times [\underline{s}, \overline{s}],$$

where the function v^* is the same as in (6.78), then there exists at most one function $c^*(x)$.

Brief Outline of the Proof. We outline the proof only briefly because it is simple. Uniqueness of the problem (6.97), (6.98) is obvious. Having uniquely determined the function p^*, we uniquely find the function $V^*(x,\overline{s})$ via (6.92). Substitute this function $V^*(x,\overline{s})$ in (6.91). Next, applying the Carleman estimate of Lemma 6.5.1, we obtain uniqueness of the function $q^*(x,s)$. The s integrals are not a problem, as it is clear from Sect. 1.10. □

6.7 The Third Approximate Global Convergence Theorem

Just as in (2.120) (Sect. 2.8.2), assume that

$$\overline{s} > 1, \ \lambda h \geq 1, \tag{6.102}$$

where $\lambda > 1$ is the parameter of the CWF (2.38). As in (2.121), we obtain from (6.102) that

$$\max_{1 \leq n \leq N} \{|A_{1,n}| + |A_{2,n}|\} \leq 8\overline{s}^2. \tag{6.103}$$

In general, embedding theorems are valid for domains with sufficiently smooth boundaries. It follows from Lemma 1 of §4 of Chap. 3 of the book [127] that if Q is a rectangular prism, then any function $f \in H^k(Q)$ can be extended in a bigger rectangular prism $Q_1 \supset Q$, $\partial Q \cap \partial Q_1 = \varnothing$ as the function $f_1 \in H^k(Q_1)$, $f_1(x) = f(x)$ in Q and $\|f_1\|_{H^k(Q_1)} \leq Z \|f\|_{H^k(Q)}$, where the constant $Z = Z(Q, Q_1) > 0$. Hence, embedding theorems are valid for rectangular prisms. Hence,

$$\|f\|_{C^3(\overline{\Omega})} \leq C \|f\|_{H^5(\Omega)}, \forall f \in H^5(\Omega). \tag{6.104}$$

Let the domain Ω be the same as in Sect. 6.5. Recall that $\Omega_\varkappa \subset \Omega$ for $\varkappa \in (1/3, 1)$ and $\Omega_1 = \Omega$. Following the construction of Sect. 6.4.1, we assume that

$$P_2 = \text{const.} \in \left(\frac{1}{3}, 1\right), \ c(x) = 1 \text{ for } x \in \mathbb{R}^3 \backslash \Omega_{P_2}, \tag{6.105}$$

$$\Omega' \subset \Omega_{P_2}, \ \partial\Omega' \cap \partial\Omega_{P_2} = \varnothing. \tag{6.106}$$

Recall that functions $\widehat{c}_{n,k}(x)$ are defined via (6.19). Since $\widehat{c}_{n,k}(x) \neq c_{n,k}(x)$ for $x \in \Omega_{P_2} \backslash \Omega'$, then the number $\text{meas}(\Omega_{P_2} \backslash \Omega')$ can be considered as a part of the error in the data. Hence, we assume that the domain Ω' is such that

$$\text{meas}\left(\Omega_{P_2}\backslash\Omega'\right) < \frac{\varepsilon}{2}, \tag{6.107}$$

where $\varepsilon \in (0,1)$ is sufficiently small. Since by construction $\widehat{c}_{n,k}(x), c^*(x) \in [1,d], \forall x \in \mathbb{R}^3$, and $\widehat{c}_{n,k}(x) = c_{n,k}(x), \forall x \in \Omega'$, then by (6.34), (6.105), and (6.107),

$$\|\widehat{c}_{n,k} - c^*\|_{L_2(\Omega)} \leq \|c_{n,k} - c^*\|_{L_2(\Omega')} + d\varepsilon \leq \|\overline{c}_{n,k} - c^*\|_{L_2(\Omega')} + d\varepsilon. \tag{6.108}$$

As it is always the case in the convergence analysis of ill-posed problems (see Chaps. 1, 2, and 4), we need to connect the regularization parameter α of the QRM in (6.43) with various approximation errors. Those errors are the level of the error σ in the data (Lemma 6.7), the grid step size h in the s-direction, and the number ε in (6.107).

As it was stated in Sect. 6.1, the major difficulty in applying the QRM to the nonlinear case is caused by many iterations rather than by a single iteration in the linear case. More precisely, to ensure the stability of our process, we need to iteratively "suppress" the large parameter α^{-b_1} in (6.71). In addition, we need to estimate tails. These are two reasons of imposing a smallness assumption on the length $\beta = \overline{s} - \underline{s} = Nh$, where $N \geq 1$ is an integer. The latter is similar with Theorems 2.8.2 and 2.9.4.

For a number $x > 0$, let $\{x\}^\circ$ denotes such an integer that $x - \{x\}^\circ \in [0,1)$. Thus, we impose the following conditions:

$$\sigma, \varepsilon \in \left(0, \sqrt{\alpha}\right), \tag{6.109}$$

$$h = \sqrt{\alpha},\ \beta := \beta(\alpha) = \sqrt{\alpha}\{f(\alpha)\}^\circ := \sqrt{\alpha}N, \tag{6.110}$$

where the function $f(\alpha)$ is monotonically decreasing for $\alpha \in (0,1)$,

$$f(\alpha) > 0 \text{ for } \alpha \in (0,1), \lim_{\alpha \to 0^+} f(\alpha) = \infty \text{ and } \lim_{\alpha \to 0^+} \frac{f(\alpha)}{\ln(\alpha^{-1})} = 0. \tag{6.111}$$

Two examples of the function $f(\alpha)$ are

$$f_1(\alpha) = \left[\ln\left(\alpha^{-1}\right)\right]^r, r = \text{const.} \in (0,1)$$

and

$$f_2(\alpha) = \ln\left(\ln\left(\alpha^{-1}\right)\right).$$

Recall that the number of iterations can be one of regularization parameters for an ill-posed problem. On the other hand, one might also have a vector of regularization parameters. Therefore, one can consider (6.109), (6.110), and (6.111) as the linkage between regularization parameters $(\alpha, N) := (\alpha, N(\alpha))$ between themselves as well as with "error" parameters (σ, ε, h).

Let $(q_{n,k}, \overline{c}_{n,k}, V_{n,k})$ be the triple computed on a certain step of our iterative process of Sect. 6.4.3. Denote

$$\widetilde{q}_{n,k} = q_{n,k} - q_n^*,\ \widetilde{c}_{n,k} = \overline{c}_{n,k} - c^*,\ \widetilde{V}_{n,k} = V_{n,k} - V^*.$$

Similarly for $\widetilde{q}_n, \widetilde{c}_n, \widetilde{V}_n$. Note that since the function $c^* \in [1,d]$, then (6.34) implies that

$$|c_{n,k}(x) - c^*(x)| \leq |\overline{c}_{n,k}(x) - c^*(x)| = |\widetilde{c}_{n,k}(x)|,\ x \in \Omega. \tag{6.112}$$

Even though we have assumed (for brevity only) that there is no error in functions of (6.90), Lemma 6.7 and Theorem 6.7 "allow" error to be present in functions $\psi_0^*(x,\overline{s}), \psi_1^*(x,\overline{s})$ in (6.98).

Lemma 6.7 (estimate of $\widetilde{\mathbf{V}}_{1,1}$). *Let the domain Ω be as in (6.44) and the source $x_0 \notin \overline{\Omega}$. Let assumptions 1–3 of Sect. 6.6.2 hold as well as (6.109). Let $\Psi^* \in H^5(\Omega)$ be a function satisfying boundary conditions (6.98). Suppose that there exists a function $\Psi \in H^5(\Omega)$ satisfying boundary conditions (6.80). Let the number $\sigma \in (0,1)$ be the level of the error in the function Ψ^* when it is replaced with the function Ψ, $B = B(\Omega, \overline{s}, d, x_0) > 2$ be the constant of Theorem 2.9.1.1 and*

$$\|\Psi - \Psi^*\|_{H^5(\Omega)} \leq \sigma \leq \sqrt{\alpha}, \tag{6.113}$$

$$\|p^*\|_{H^5(\Omega)} \leq B. \tag{6.114}$$

Let the function $p = p(x;\alpha) \in H^5(\Omega)$ be the unique QRM solution of the problem (6.99), (6.100) which is guaranteed by Lemma 6.5.2. Let the tail function $V_{1,1}(x) := V_{1,1}(x;\alpha)$ has the form (6.101). Then for every $\alpha \in (0,1)$,

$$\left\|\nabla \widetilde{V}_{1,1}\right\|_{L_2(\Omega)} + \left\|\Delta \widetilde{V}_{1,1}\right\|_{L_2(\Omega)} \leq B\sqrt{\alpha}, \tag{6.115}$$

$$\|\nabla V_{1,1}\|_{C(\overline{\Omega})} \leq B. \tag{6.116}$$

Proof. Note that the existence of the function Ψ^* follows from the assumed existence of the function p^* satisfying conditions (6.97), (6.98). Likewise the trace theorem, (6.113), (6.98), and (6.100) imply that

$$\|\psi_0^*(x,\overline{s}) - \psi_0(x,\overline{s})\|_{H^1(\Gamma_1)} + \|\psi_1^*(x,\overline{s}) - \psi_0(x,\overline{s})\|_{L_2(\Gamma_1)} \leq C\frac{\sigma}{\overline{s}^2},$$

where $C = C(\Omega) > 0$ is a constant. This means that the error is introduced in the boundary data $\psi_0^*(x,\overline{s}), \psi_1^*(x,\overline{s})$ and its level is proportional to $\sigma \in \left(0, \sqrt{\alpha}\right)$. For brevity, we do not put in this proof the dependence of the function p from α.

Denote

$$\widetilde{p}(x) = (p - \Psi)(x) - \left(p^* - \Psi^*\right)(x).$$

Then the function $\widetilde{p}(x)$ satisfies zero boundary conditions (6.100) and

$$(\Delta\widetilde{p}, \Delta v) + \alpha [\widetilde{p}, v] = \left(\Delta\Psi^* - \Delta\Psi, \Delta v\right) + \alpha \left[\Psi^* - \Psi, v\right] + \alpha \left[p^*, v\right],$$

for all functions $v \in H^5(\Omega)$ satisfying zero boundary conditions (6.100). Setting here $v := \widetilde{p}$, and using (6.109), (6.113), and (6.114), we obtain

$$\|\Delta\widetilde{p}\|^2_{L_2(\Omega)} + \alpha \|\widetilde{p}\|^2_{H^5(\Omega)} \leq \alpha B^2. \tag{6.117}$$

Estimate $\|\Delta\widetilde{p}\|^2_{L_2(\Omega)}$ in (6.117) from the below. We have

$$(\Delta\widetilde{p})^2 = \left(\widetilde{p}^2_{xx} + \widetilde{p}^2_{yy} + \widetilde{p}^2_{zz}\right) + 2\widetilde{p}_{xx}\widetilde{p}_{yy} + 2\widetilde{p}_{xx}\widetilde{p}_{zz} + 2\widetilde{p}_{yy}\widetilde{p}_{zz}, \tag{6.118}$$

$$2\widetilde{p}_{xx}\widetilde{p}_{yy} = \partial_x\left(2\widetilde{p}_x\widetilde{p}_{yy}\right) - 2\widetilde{p}_x\widetilde{p}_{yyx} = \partial_x\left(2\widetilde{p}_x\widetilde{p}_{yy}\right) + \partial_y\left(-2\widetilde{p}_x\widetilde{p}_{xy}\right) + 2\widetilde{p}^2_{xy},$$

$$2\widetilde{p}_{xx}\widetilde{p}_{zz} = \partial_x\left(2\widetilde{p}_x\widetilde{p}_{zz}\right) - 2\widetilde{p}_x\widetilde{p}_{zzx} = \partial_x\left(2\widetilde{p}_x\widetilde{p}_{zz}\right) + \partial_z\left(-2\widetilde{p}_x\widetilde{p}_{xz}\right) + 2\widetilde{p}^2_{xz},$$

and similarly for $2\widetilde{p}_{yy}\widetilde{p}_{zz}$. Integrate (6.118) over Ω using these formulas for products. Since by (6.98) and (6.100) $\partial_n\widetilde{p}\ |_{\partial\Omega} = 0$, then boundary integrals will be equal zero. Next, use

$$\widetilde{p}_x(x, y, z) = \int\limits_{-1/4}^{x} \widetilde{p}_{xx}(\xi, y, z)\, d\xi$$

and similar formulas for $\widetilde{p}_y, \widetilde{p}_z$. Using (6.117), we obtain

$$\alpha B^2 \geq \|\Delta\widetilde{p}\|^2_{L_2(\Omega)} \geq \sum_{|\alpha|=2} \|D^\alpha\widetilde{p}\|^2_{L_2(\Omega)} \geq C \|\nabla\widetilde{p}\|^2_{L_2(\Omega)}.$$

This, (6.92), (6.101), (6.113), and (6.114) imply (6.115). Next, by (6.104), (6.109), (6.113) (6.114), and (6.117) $\|\nabla p\|_{C(\overline{\Omega})} \leq C \|p\|_{H^5(\Omega)} \leq B$. This estimate combined with (6.101) imply (6.116). □

Theorem 6.7 claims approximate global convergence property of the algorithm of Sects. 6.4.3 and 6.4.4 in the framework of the third approximate mathematical model.

Theorem 6.7. *Let the following conditions hold: ones of Sect. (6.81), (6.90), ones of Lemma 6.7, as well as (6.102), (6.105), (6.106),(6.107), (6.109), (6.110), and (6.111). Let the number $\beta \in (P_2, 1)$, m be the number of inner iterations for functions $q_{n,k}$, $k \in [1, m]$ and f be the function in (6.110), (6.111). Then there exists a constant $D = D(\overline{s}, d, x_0, C^*, f, P_2, \beta) > 1$, numbers*

$$b_1 = b_1\left(\overline{s}, d, x_0, C^*, f, P_2, \beta\right) \in \left(0, \frac{1}{2}\right),\ b_2 = \frac{1}{2} - b_1$$

defined in (6.69) and (6.70) and a sufficiently small $\alpha_0 = \alpha_0(\overline{s}, d, x_0, C^*, f, P_2, \beta, m, N) \in (0,1)$ *such that the following estimates are valid:*

$$\|c_n - c^*\|_{L_2(\Omega_1)} \leq \alpha^{b_2/2},\ \forall (n,\alpha) \in [1,N] \times (0,\alpha_0). \tag{6.119}$$

Thus, the iterative process of Sects. 6.4.3 and 6.4.4 is approximately globally convergent of the level $\alpha^{b_2/2}$ *in the framework of the third approximate mathematical model.*

Proof. In this proof, $B = B(\Omega, \overline{s}, d, x_0) > 2$ is the constant of Theorem 2.9.1.1. A combination of Theorem 2.7.2 with (6.5), (6.18), (6.19), (6.20), (6.34), (6.35), (6.36), and (6.37) guarantees the existence and uniqueness of tails $V_{n,k}$. Note that because of (6.79) and (6.80), the estimate (6.82) does not change when the number N of subintervals of the interval $[\underline{s}, \overline{s}]$ increases with the decrease of the parameter α. Let $(n,k) \in [1,N] \times [1,m]$.

Assuming that the constant D is found, we first estimate the number $D^{2Nm+4}\alpha^{b_2}$. Using (6.110) and (6.111), we obtain that there exists a sufficiently small number

$$\alpha_0 = \alpha_0\left(\overline{s}, d, x_0, C^*, f, P_2, \beta, m, N\right) \in (0,1),$$

such that for all $\alpha \in (0, \alpha_0)$,

$$D^{2Nm+4}\alpha^{b_2} \leq D^4 \exp\left\{-\ln\left(\alpha^{-1}\right)\left[b_2 - 2m \ln D \frac{f(\alpha)}{\ln(\alpha^{-1})}\right]\right\} < \alpha^{b_2/2}. \tag{6.120}$$

Below, in this proof, $\alpha \in (0, \alpha_0)$. It follows from (6.120) that it is sufficient to prove that

$$\|c_n - c^*\|_{L_2(\Omega')} \leq D^{2nm}\alpha^{b_2},\ \forall (n,\alpha) \in [1,N] \times (0,\alpha_0). \tag{6.121}$$

By (6.26), (6.28), (6.40), (6.85), (6.87), (6.90), and (6.96), the function $\widetilde{q}_{n,k}$ is the QRM solution of the following problem:

$$\Delta \widetilde{q}_{n,k} - A_{1,n}\left(\chi_2(x) h \sum_{j=0}^{n-1} \nabla q_j - \nabla V_{n,k}\right) \nabla \widetilde{q}_{n,k} = \widetilde{H}_{n,k}, \tag{6.122}$$

$$\widetilde{q}_{n,k}\,|_{\Gamma_1} = \partial_{x_3}\widetilde{q}_{n,k}\,|_{\Gamma_1} = \partial_n \widetilde{q}_{n,k}\,|_{\Gamma_2 \cup \Gamma_3} = 0, \tag{6.123}$$

where

$$\widetilde{H}_{n,k}(x) = -A_{1,n}\left(\chi_2(x) h \sum_{j=0}^{n-1} \nabla \widetilde{q}_j - \nabla \widetilde{V}_{n,k}\right) \nabla q_n^*$$

$$-A_{2,n}\left(\chi_2(x) h \sum_{j=0}^{n-1} \nabla \widetilde{q}_j\right)\left(h \sum_{j=0}^{n-1}\left(\nabla q_j + \nabla q_j^*\right) - 2\nabla V_{n,k}\right)$$

$$+A_{2,n}\nabla\widetilde{V}_{n,k}\left(2\chi_2(x)\,h\sum_{j=0}^{n-1}\nabla q_j^* - \left(\nabla V_{n,k}+\nabla V^*\right)\right)$$
$$-(1-\chi_2(x))\,h\sum_{j=0}^{n-1}\nabla q_j^*\left(-A_{1,n}\nabla q_n^* + A_{2,n}h\sum_{j=0}^{n-1}\nabla q_j^* - 2A_{2,n}\nabla V_{n,k}^*\right). \tag{6.124}$$

Let $Q_n(x)$ be the last line of (6.124). We now estimate this function using Theorem 2.9.1.1, (6.81), (6.83), (6.103), (6.110), (6.111), and (6.116):

$$\|Q_n\|_{L_2(\Omega)} \le 8\overline{s}^2 C^*\sqrt{\alpha}\,f(\alpha)\left(C^*+\sqrt{\alpha}\,f(\alpha)+B\right) \le \alpha^{b_2},\ n\in[1,N]. \tag{6.125}$$

First, we estimate $\widetilde{q}_{1,1}$. Denote

$$G_{1,1}\widetilde{q}_{1,1} := \Delta\widetilde{q}_{1,1} + A_{1,1}\nabla V_{1,1}\nabla\widetilde{q}_{n,k}.$$

The function $\widetilde{q}_{1,1}$ satisfies boundary conditions (6.123). In addition, since $\widetilde{q}_{1,1}$ is the QRM solution of the problem (6.122), (6.123), (6.124) for $(n,k)=(1,1)$, then the following integral identity holds for all functions $v\in H^5(\Omega)$ satisfying (6.123):

$$\left(G_{1,1}\widetilde{q}_{1,1}, G_{1,1}v\right) + \alpha\left[\widetilde{q}_{1,1}, v\right] = \left(\widetilde{H}_{1,1}, G_{1,1}v\right) - \alpha\left[q_1^*, v\right],$$
$$\widetilde{H}_{1,1} := A_{1,1}\nabla\widetilde{V}_{1,1}\nabla q_n^* - A_{2,n}\nabla\widetilde{V}_{1,1}\left(\nabla V_{1,1}+\nabla V^*\right) + Q_1. \tag{6.126}$$

By (2.195), (Theorem 2.9.1.1), and (6.103), $\|A_{1,1}\nabla V_{1,1}\|_{C(\overline{\Omega})} \le 8B\overline{s}^2$. Hence, using Lemma 6.5.3, Theorem 6.5, and (6.83), we obtain

$$\|\widetilde{q}_{1,1}\|_{H^5(\Omega)} \le D\left(\alpha^{-1/2}\left\|\widetilde{H}_{1,1}\right\|_{L_2(\Omega)}+1\right), \tag{6.127}$$

$$\|\widetilde{q}_{1,1}\|_{H^2(\Omega_{P_2})} \le D\left(\alpha^{-b_1}\left\|\widetilde{H}_{1,1}\right\|_{L_2(\Omega)}+\alpha^{b_2}\right). \tag{6.128}$$

Estimate now the norm $\left\|\widetilde{H}_{1,1}\right\|_{L_2(\Omega)}$. By (2.195), (Theorem 2.9.1.1), (6.83), (6.103), (6.115), (6.116), (6.125), and (6.126),

$$\left\|\widetilde{H}_{1,1}\right\|_{L_2(\Omega)} \le 8\overline{s}^2 C^* B\alpha^{b_2} + 16\overline{s}^2 B\alpha^{b_2} + \alpha^{b_2} \le 8\overline{s}^2 B\left(C^*+3\right)\alpha^{b_2}.$$

We choose such a constant D that

$$D \ge 8\overline{s}^2 B\left(C^*+6\right). \tag{6.129}$$

Hence,

$$\left\|\widetilde{H}_{1,1}\right\|_{L_2(\Omega)} \le D\alpha^{b_2}.$$

Hence, using (6.127), (6.128). (6.129), and $b_2 = 1/2 - b_1$, we obtain

$$\|\widetilde{q}_{1,1}\|_{H^5(\Omega)} \leq D^2\left(\alpha^{-b_1}+1\right), \tag{6.130}$$

$$\|\widetilde{q}_{1,1}\|_{H^2(\Omega_{P_2})} \leq D^2\left(\alpha^{1/2-2b_1}+\alpha^{b_2}\right). \tag{6.131}$$

Since $q_{1,1} = \widetilde{q}_{1,1} + q_1^*$, then (6.83), (6.104), and (6.130) lead to

$$\|q_{1,1}\|_{C^1(\overline{\Omega})} \leq D^3\left(\alpha^{-b_1}+2\right). \tag{6.132}$$

We now estimate $\|\widetilde{c}_{1,1}\|_{L_2(\Omega')}$. It follows from (6.32), (6.33), (6.88), (6.89), and (6.90) that

$$\begin{aligned}\widetilde{c}_{1,1} = &\left(-h\Delta\widetilde{q}_{1,1} + \Delta\widetilde{V}_{1,1}\right)\\ &+s_1^2\left(-h\nabla\widetilde{q}_{1,1} + \nabla\widetilde{V}_{1,1}\right)\left[-h\nabla\left(q_{11}+q_1^*\right) + \nabla\left(V_{11}+V^*\right)\right].\end{aligned} \tag{6.133}$$

By (6.120),

$$D^{2Nm+4}\alpha^{b_2} < N^{-1}. \tag{6.134}$$

Hence, (6.83), (6.104), (6.110), (6.129), (6.130), (6.131), (6.132), and (6.134) imply that

$$h\left\|\Delta\widetilde{q}_{1,1}\right\|_{L_2(\Omega_{P_2})}, h\left\|\nabla\widetilde{q}_{1,1}\right\|_{L_2(\Omega_{P_2})} \leq 2D^2\alpha^{2b_2} \leq D^3\alpha^{2b_2} \leq \alpha^{b_2}N^{-1}, \tag{6.135}$$

$$h\left(\|\nabla q_{1,1}\|_{C(\overline{\Omega})} + 2\left\|\nabla q_1^*\right\|_{C(\overline{\Omega})}\right) \leq D^3\left(\alpha^{b_2}+4\alpha^{1/2}\right) \leq N^{-1}. \tag{6.136}$$

Next, by (2.195), (Theorem 2.9.1.1), and (6.116), $\|\nabla\left(V_{11}+V^*\right)\|_{C(\overline{\Omega})} \leq 2B$. Hence, using (6.129) and (6.136), we obtain

$$s_1^2\left\|-h\nabla\left(q_{1,1}+q_1^*\right) + \nabla\left(V_{1,1}+V^*\right)\right\|_{C(\overline{\Omega})} \leq D.$$

Hence, (6.115), (6.129), (6.133), and (6.135) imply that

$$\|\widetilde{c}_{1,1}\|_{L_2(\Omega')} \leq \|\widetilde{c}_{1,1}\|_{L_2(\Omega_{P_2})} \leq \left(B+N^{-1}\right)(D+1)\,\alpha^{b_2} \leq D^2\alpha^{b_2}. \tag{6.137}$$

Hence, (2.196), (Theorem 2.9.1.1), (6.108), (6.109), (6.129), and (6.137) lead to

$$\left\|\nabla\widetilde{V}_{1,2}\right\|_{L_2(\Omega)} + \left\|\Delta\widetilde{V}_{1,2}\right\|_{L_2(\Omega)} \leq D^3\alpha^{b_2}. \tag{6.138}$$

We have obtained estimates (6.130)–(6.132), (6.135), (6.136), (6.137) and (6.138) starting from the estimates (6.115), and (6.116) for functions $\widetilde{V}_{1,1}, V_{1,1}, V^*$. Hence, continuing this process m times, using $q_1 = q_{1,m}, c_1 = c_{1,m}$, and keeping in mind that by (6.38) $V_{2,1} = V_{1,m+1}$, we obtain similarly with (6.135)–(6.138)

$$h\left\|\nabla\widetilde{q}_1\right\|_{L_2(\Omega_{P_2})}, h\left\|\Delta\widetilde{q}_1\right\|_{L_2(\Omega_{P_2})} \leq \alpha^{b_2}N^{-1}, \tag{6.139}$$

$$h\left(\left\|\nabla q_1\right\|_{C(\overline{\Omega})} + 2\left\|\nabla q_1^*\right\|_{C(\overline{\Omega})}\right) \leq N^{-1}, \tag{6.140}$$

$$\left\|c_1 - c^*\right\|_{L_2(\Omega')} \leq \left\|\widetilde{c}_{1,m}\right\|_{L_2(\Omega')} \leq D^{2m}\alpha^{b_2}, \tag{6.141}$$

$$\left\|\nabla\widetilde{V}_{2,1}\right\|_{L_2(\Omega)} + \left\|\Delta\widetilde{V}_{2,1}\right\|_{L_2(\Omega)} \leq D^{2m+1}\alpha^{b_2}. \tag{6.142}$$

To obtain (6.141) from (6.137), we have used (6.112). Note that the estimate (6.141) is the estimate (6.121) for $n = 1$. Thus, Theorem 6.7 is proved for $N = 1$. Suppose now that $N \geq 2$ Without loss of generality, it is convenient to assume that $N > 2$. Let $n \in [2, N)$. Because of (6.139), (6.140), (6.141), and (6.142), we assume that

$$h\sum_{j=0}^{n-1}\left\|\nabla\widetilde{q}_j\right\|_{L_2(\Omega_{P_2})}, h\sum_{j=0}^{n-1}\left\|\Delta\widetilde{q}_j\right\|_{L_2(\Omega_{P_2})} \leq \frac{n-1}{N}\alpha^{b_2}, \tag{6.143}$$

$$h\sum_{j=0}^{n-1}\left(\left\|\nabla q_j\right\|_{C(\overline{\Omega})} + 2\left\|\nabla q_j^*\right\|_{C(\overline{\Omega})}\right) \leq \frac{n-1}{N}, \tag{6.144}$$

$$\left\|\nabla\widetilde{V}_{n,1}\right\|_{L_2(\Omega_{P_2})} + \left\|\Delta\widetilde{V}_{n,1}\right\|_{L_2(\Omega_{P_2})} \leq D^{2(n-1)m+1}\alpha^{b_2}, \tag{6.145}$$

$$\left\|c_{n-1} - c^*\right\|_{L_2(\Omega')} \leq \left\|\widetilde{c}_{n-1,m}\right\|_{L_2(\Omega_{P_2})} \leq D^{2(n-1)m}\alpha^{b_2}. \tag{6.146}$$

Denote

$$D^{2(n-1)m+1}\alpha^{b_2} := D_{n-1}\alpha^{b_2}. \tag{6.147}$$

We are going to prove now (6.143), (6.144), (6.145), (6.146), and (6.121) for $n := n + 1$. Because of (6.122), denote

$$G_{n,1}\widetilde{q}_{n,1} = \Delta\widetilde{q}_{n,1} - A_{1,n}\left(\chi_2(x)\, h\sum_{j=0}^{n-1}\nabla q_j - \nabla V_{n,1}\right)\nabla\widetilde{q}_{n,1}. \tag{6.148}$$

The function $\widetilde{q}_{n,1}$ satisfies boundary conditions (6.123) as well as the following integral identity for all functions $v \in H^5(\Omega)$ satisfying boundary conditions (6.123):

$$\left(G_{n,1}\widetilde{q}_{n,1}, G_{n,1}v\right) + \alpha\left[\widetilde{q}_{n,1}, v\right] = \left(\widetilde{H}_{n,1}, G_{n,1}v\right) - \alpha\left[q_n^*, v\right]. \tag{6.149}$$

Estimate the coefficient at $\nabla\widetilde{q}_{n,1}$ in (6.148). Using (2.195), (Theorem 2.9.1.1), (6.103), and (6.144), we obtain:

$$\left|A_{1,n}\left(\chi_2(x)\, h\sum_{j=0}^{n-1}\nabla q_j - \nabla V_{n,1}\right)\right| \leq 16B\overline{s}^2. \tag{6.150}$$

In terms of Theorem 6.5, an important feature of (6.150) is that this estimate is independent on n. Hence, the same constants $D, b_1, b_2 = 1/2 - b_1$ can be used in (6.151), (6.152) for all $n \in [2, N)$. Thus, using Lemma 6.5.3, Theorem 6.5, (6.129), (6.149), and (6.150), we obtain

$$\|\widetilde{q}_{n,1}\|_{H^5(\Omega)} \leq D\left(\alpha^{-1/2}\left\|\widetilde{H}_{n,1}\right\|_{L_2(\Omega)} + 1\right), \tag{6.151}$$

$$\|\widetilde{q}_{n,1}\|_{H^2(\Omega_{P_2})} \leq D\left(\alpha^{-b_1}\left\|\widetilde{H}_{n,1}\right\|_{L_2(\Omega)} + \alpha^{b_2}\right). \tag{6.152}$$

Hence, using (6.79), (6.80), (6.103), (6.104), (6.124), (6.125), (6.129), (6.143)–(6.147), Theorem 2.9.1.1, and that $B > 2$, we obtain

$$\begin{aligned}\left\|\widetilde{H}_{n,1}\right\|_{L_2(\Omega)} &\leq 8\overline{s}^2\left(\frac{n-1}{N}\alpha^{b_2} + D_{n-1}\alpha^{b_2}\right)C^* + 8\overline{s}^2\frac{n-1}{N}\alpha^{b_2}\left(\frac{n-1}{N} + 2B\right)\\ &\quad + 8\overline{s}^2 D_{n-1}\alpha^{b_2}\left(2\frac{n-1}{N} + 2B\right) + \alpha^{b_2}\\ &\leq 8\overline{s}^2 D_{n-1}\alpha^{b_2}\left(3 + 4B + \frac{3}{2}C^*\right) \leq DD_{n-1}\alpha^{b_2}.\end{aligned}$$

Hence, (6.104), (6.134), (6.145), (6.151), and (6.152) imply that

$$h\left(\|\nabla q_{n,1}\|_{C(\overline{\Omega})} + 2\left\|\nabla q^*_{n,1}\right\|_{C(\overline{\Omega})}\right) \leq D^3 D_{n-1}\alpha^{b_2} \leq D^{2Nm+4}\alpha^{b_2} \leq N^{-1}, \tag{6.153}$$

$$h\,\|\widetilde{q}_{n,1}\|_{H^2(\Omega_{P_2})} \leq D\left(DD_{n-1}\alpha^{2b_2} + \alpha^{b_2+1/2}\right) \leq D^{2Nm+4}\alpha^{2b_2} \leq \alpha^{b_2}N^{-1}. \tag{6.154}$$

We obtain similarly with (6.133)

$$\begin{aligned}\widetilde{c}_{n,1} &= -h\Delta\widetilde{q}_{n,1} - h\sum_{j=0}^{n-1}\Delta\widetilde{q}_j + \Delta\widetilde{V}_{n,1}\\ &\quad + s_n^2\left(-h\nabla\widetilde{q}_{n,1} - h\sum_{j=0}^{n-1}\nabla\widetilde{q}_j + \nabla\widetilde{V}_{n,1}\right)\\ &\quad \cdot\left(-h\nabla\left(q_{n,1} + q_n^*\right) - h\sum_{j=0}^{n-1}\nabla\left(q_j + q_j^*\right) + \nabla\left(V_{n,1} + V^*\right)\right).\end{aligned}$$

Hence, using (6.129), (6.143)–(6.145), (6.153), and (6.154), we obtain

$$\|\widetilde{c}_{n,1}\|_{L_2(\Omega_{P_2})} \leq \left(\frac{n}{N}\alpha^{b_2} + D_{n-1}\alpha^{b_2}\right)\left[1 + \overline{s}^2\left(\frac{n}{N} + B\right)\right] \leq DD_{n-1}\alpha^{b_2}.$$

Hence, (2.196), (Theorem 2.9.1.1), (6.108), and (6.109) imply that

$$\left\|\nabla \widetilde{V}_{n,2}\right\|_{L_2(\Omega)} + \left\|\Delta \widetilde{V}_{n,2}\right\|_{L_2(\Omega)} \leq D^2 D_{n-1}\alpha^{b_2}.$$

Similarly for $k = 1, \ldots, m$,

$$\|\widetilde{c}_{n,k}\|_{L_2(\Omega_{P_2})} \leq D^{2k-1} D_{n-1}\alpha^{b_2},$$

$$\left\|\nabla \widetilde{V}_{n,k+1}\right\|_{L_2(\Omega)} + \left\|\Delta \widetilde{V}_{n,k+1}\right\|_{L_2(\Omega)} \leq D^{2k} D_{n-1}\alpha^{b_2}.$$

Hence, similarly with the above, we obtain that estimates (6.153), (6.154) are valid for functions $q_{n,k}, \widetilde{q}_{n,k}$.This implies the validity of (6.143) and (6.144) for $n := n + 1$. Similarly,

$$\|c_{n,k} - c^*\|_{L_2(\Omega')} \leq \|\widetilde{c}_{n,k}\|_{L_2(\Omega_{P_2})} \leq D^{2k} D_{n-1}\alpha^{b_2} = D^{2(n-1)m+2k}\alpha^{b_2}, k \in [1, m],$$

$$\left\|\nabla \widetilde{V}_{n,m+1}\right\|_{L_2(\Omega)} + \left\|\Delta \widetilde{V}_{n,m}\right\|_{L_2(\Omega)} \leq D^{2m} D_{n-1}\alpha^{b_2} = D^{2nm+1}\alpha^{b_2}.$$

The last two estimates establish (6.145) and (6.146) for $n := n + 1$. □

6.8 Numerical Studies

6.8.1 *Main Discrepancies Between Convergence Analysis and Numerical Implementation*

It is well known that some discrepancies between the convergence analysis and numerical implementations are almost inevitable for both well-posed and ill-posed problems. The main reason is that because of the complicated structure of those problems, the theory usually can grasp only a part of numerical studies rather than all aspects. For example, as it was pointed out in Sect. 2.10, constants in convergence theorems usually are significantly overestimated (maybe with the only exception of a few very simple linear problems).

We now list main discrepancies between the above convergence analysis of this chapter and the numerical implementation for our specific case. Some of these discrepancies are the same as ones named in Sect. 3.1.2. The *first* main discrepancy is with regard to Lemma 2.3 about a sufficient condition of the regularity of geodesic lines. In general, an easily verifiable condition of this sort is unknown, except of the trivial case when the function $c(x)$ is close to a constant. On the other hand, the authors are unaware about any reasonable results for CIPs for hyperbolic PDEs without either the assumption of the regularity of geodesic lines or a somewhat close assumption. We verify the asymptotic behavior of Lemma 2.3 computationally; see Sect. 3.1.2.

The *second* main discrepancy is that we replace in our computations $\alpha \|u\|^2_{H^5(\Omega)}$ in (6.43) with $\alpha \|u\|^2_{H^2(\Omega)}$, because the latter is simpler to implement numerically. One of the reasons why this works computationally is that we deal with finite dimensional spaces whose dimensions are not exceedingly large. Recall that all norms are equivalent in such spaces.

The *third* main discrepancy is that we conduct computations for the case when the point source in (6.2) is replaced with the plane wave. This is because the case of the plane wave is reasonable for our target application to imaging of plastic land mines, since the wave radiated by a point source effectively becomes a pane wave when that source is located far from the domain of interest. We have chosen the point source in (6.2) only because we wanted to use Lemma 2.3. Other than this, the above technique can be easily extended to the case of the plane wave.

The *fourth* main discrepancy is that we have ignored in our computations the function $\chi_2(x)$ in Sects. 6.4.2 and 6.4.3. Indeed, this function was introduced only for the sake of the convergence analysis.

6.8.2 A Simplified Mathematical Model of Imaging of Plastic Land Mines

The first main simplification of our model is that we consider the 2D case instead of 3D, although a 3D numerical test is also presented below. Second, we ignore the air/ground interface, assuming that the governing PDE is valid on the entire 2D plane. Results of Sect. 6.9 indicate that the influence of the air/ground interface can be handled via a data pre-processing procedure.

Let the ground be $\{\mathbf{x} = (x, z) : z > 0\} \subset \mathbb{R}^2$. Suppose that a polarized electric field is generated by a plane wave, which is initialized at the line $\left\{z = z^0 < 0, x \in \mathbb{R}\right\}$ at the moment of time $t = 0$. The following hyperbolic equation can be derived from the Maxwell's equations in the 2D case:

$$\varepsilon_r(\mathbf{x}) u_{tt} = \Delta u, \ (\mathbf{x}, t) \in \mathbb{R}^2 \times (0, \infty), \tag{6.155}$$

$$u(\mathbf{x}, 0) = 0, \ u_t(\mathbf{x}, 0) = \delta\left(z - z^0\right), \tag{6.156}$$

where the function $u(\mathbf{x}, t)$ is a component of the electric field and $\varepsilon_r(\mathbf{x})$ is the spatially distributed dielectric constant. We assume that the function $\varepsilon_r(\mathbf{x})$ satisfies conditions (6.3) and (6.4) in 2D. Let the function $w_0(z, s)$,

$$w_0(z, s) = \frac{\exp\left(-s|z - z_0|\right)}{2s}, \tag{6.157}$$

be the one which corresponds to the Laplace transform (6.11) of the incident plane wave with $\varepsilon_r(\mathbf{x}) \equiv 1$. Applying the Laplace transform (6.11) to the function u in (6.155), we obtain the following analog of the problem (6.12), (6.13)

$$\Delta w - s^2 \varepsilon_r(\mathbf{x}) w = -\delta\left(z - z^0\right),\ s \geq \underline{s} = \text{const.} > 0, \mathbf{x} \in \mathbb{R}^2, \tag{6.158}$$

$$\lim_{|\mathbf{x}| \to \infty} (w - w_0)(\mathbf{x}, s) = 0. \tag{6.159}$$

It is well known that the maximal depth of an antipersonnel land mine does not exceed about 10 centimeters (cm) = 0.1 meter (m). So, we model these mines as small squares with the 0.1 m length of sides, and their centers are at the depth of 0.1 m or less. We set

$$\widetilde{\Omega} = \{\mathbf{x} = (x, z) \in (-0.3, 0.3)\ \text{m} \times (0, 0.6)\ \text{m}\}.$$

Introducing dimensionless spatial variables $\mathbf{x}' = \mathbf{x}/(0.1m)$ without changing notations, we obtain that the domain $\widetilde{\Omega}$ is transformed in the dimensionless domain:

$$\Omega = (-3, 3) \times (0, 6).$$

6.8.3 Some Details of the Numerical Implementation

To simulate the data for our CIP, we have solved (6.158) in the truncated domain

$$G = (-4, 4) \times (-2, 8).$$

We have used the FDM to solve this forward problem. The boundary condition (6.159) was replaced with

$$(w - w_0)(\mathbf{x}, s)\ |_{\partial G} = 0. \tag{6.160}$$

In principle, one might impose radiation boundary conditions at the top and bottom sides of the rectangle G. However, our computational experience shows that this would not bring much change for the function $w(x, s)$ inside the domain Ω, since this function decays exponentially with $|\mathbf{x}| \to \infty$; also see Remark 6.3 for a relevant statement. To compare, we have also solved once the problem (6.155), (6.156) and have applied the Laplace transform (6.11) then. Imaging results were almost the same. To avoid using the δ-function numerically, we have solved the problem (6.158), (6.160) for the function $\overline{w} = w - w_0$.

We assume the knowledge of functions $\varphi_0(x, s), \varphi_1(x, s)$:

$$w\ |_{\Gamma_1} = \varphi_0(x, s), \partial_n w\ |_{\Gamma_1} = \varphi_1(x, s),\ s \in [\underline{s}, \overline{s}],$$

$$\partial_n (\ln w(x, s))\ |_{\Gamma_2 \cup \Gamma_3} = -s,\ s \in [\underline{s}, \overline{s}],$$

$$\Gamma_1 = \{\mathbf{x} = (x, z) : x \in (-3, 3), z = 0\},\ \Gamma_2 \cup \Gamma_3 = \partial\Omega \backslash \Gamma_1;$$

see (6.17) for the boundary condition at $\Gamma_2 \cup \Gamma_3$. Functions $\varphi_0(x,s)$, $\varphi_1(x,s)$ were obtained in numerical simulations when the above forward problem was solved. We have added the random noise of the 5% level to the function $\varphi_0(x,s)$ via

$$\varphi_{0,\sigma}(x_i,0,s_n) = \varphi_0(x_i,0,s_n)(1+\sigma\omega_n), \sigma = 0.05,$$

where $\{x_i\}$ are grid points of the FDM for the forward problem solution and $\omega \in (-1,1)$ is a random variable. To calculate the derivative $\partial_s\left[s^{-2}\ln\left(\varphi_{0,\sigma}/w_0\right)(x_i,0,s_n)\right]$ (to obtain the boundary data for $\widehat{q}(x_i,s_n)$), we have smoothed first values of $\overline{\varphi}_{0,\sigma}(x_i,0,s_n)$ with respect to s via cubic B-splines similarly with, for example, [73]. Next, we have used finite differences to calculate the desired derivative.

We model land mines as squares with the dimensionless length of the side 1, which means 10 cm in real dimensions. Centers of those squares are located at the depths of $z = 0.6$ and $z = 1$, which means depths of 6 cm and 10 cm in variables with dimensions. We took $\Omega_{P_2} = (-3,3)\times(0,3)$ (Sect. 6.4.1).

Tables of dielectric constants [151] show that in the dry sand $\varepsilon_r = 5$ and $\varepsilon_r = 22$ in the trinitrotoluene (TNT). Hence, the mine/background contrast is $\approx 22/5 = 4.4$. Hence, considering new parameters

$$\varepsilon_r' = \frac{\varepsilon_r}{5},\ s' = s\cdot 0.1\cdot\sqrt{5}$$

and not changing notations, we obtain

$$\varepsilon_r(\text{dry sand}) = 1,\ \varepsilon_r(\text{TNT}) = 4.4. \tag{6.161}$$

Because of (6.161), we impose $\varepsilon_r(\mathbf{x}) \in [1,8]$, $\varepsilon_r(\mathbf{x}) = 1$ outside of the rectangle Ω_{P_2}. We have modified our algorithm of Sect. 6.4 via considering functions

$$\widehat{v}(\mathbf{x},s) = \frac{1}{s^2}\ln\left[\frac{w}{w_0}(\mathbf{x},s)\right],\ \widehat{q}(\mathbf{x},s) = \partial_s\widehat{v}(\mathbf{x},s) \tag{6.162}$$

instead of

$$v(\mathbf{x},s) = \frac{\ln(w(\mathbf{x},s))}{s^2},\ q(\mathbf{x},s) = \partial_s v(\mathbf{x},s),$$

where the function $w_0(z,s)$ is the same as in (6.157). This has resulted in obvious modifications of equations of Sect. 6.4. A slight modification of Theorem 6.7 can be proved for this case.

We have observed in our computations that at the backscattering side Γ_1 of the above square Ω the ratio $(w/w_0)(x,0,s) \approx 1$ for $s > 1.2$. This means a poor sensitivity of the backscattering data to the presence of abnormalities for values of the pseudo-frequency $s > 1.2$. The best sensitivity was for $s \in [0.5, 1.2]$. Hence, one should expect that the modified tail function

$$\widehat{V}(\mathbf{x},\overline{s}) = V(\mathbf{x},\overline{s}) - \frac{\ln w_0(z,\overline{s})}{\overline{s}^2} \approx 0$$

for $\overline{s} > 1.2$, at least for those points $\mathbf{x}$ which are located close to Γ_1. Hence, we have chosen $\overline{s} = 1.2$ and $s \in [0.5, 1.2] := [\underline{s}, \overline{s}]$.

We note that if we would work in the original domain $\widetilde{\Omega}$ making spatial variables dimensionless as $\mathbf{x}'' = \mathbf{x}/(1m)$, then $s'' = \sqrt{5}s$ implying that $\overline{s}'' = 12 (= 1.2/0.1)$, which can be considered as a large pseudo-frequency. The latter shows that in practical computations, the above notion of sufficiently large $\overline{s}$ is actually a conditional one and depends on particular ranges of parameters at hands.

The modified QRM functional (6.43) was written in the FDM form. Its minimization was performed with respect to the values of the function $u(x)$ at grid points via the conjugate gradient method. Our regularization term was

$$\frac{\alpha}{2}\left[\|u\|^2_{H^1(\Omega)} + \|u_{xx}\|^2_{L_2(\Omega)} + \|u_{zz}\|^2_{L_2(\Omega)}\right].$$

We have chosen the regularization parameter $\alpha = 0.08$ and the spatial grid step size $h_{sp} = 0.122$. First, we have solved the problem (6.99), (6.100) via the QRM and thus have calculated the first tail $V_{1,1}(x)$ in (6.101). Next, we have continued as in Sect. 6.4 with $m := 10$. We have used the spatial grid step size $h_{sp} = 0.122$ to minimize the QRM functional (6.43) via the FDM. However, our attempt to decrease it by the factor of 2 to $h_{sp} = 0.061$ has led to a significant deterioration of computational results.

We took the grid step size in the s-direction as $h = 0.1$ and have made several sweeps over the interval $s \in [0.5, 1.2]$ as follows. Let the function $\varepsilon_r^{(1)}(\mathbf{x})$ be the approximation for the function $\varepsilon_r(\mathbf{x})$ computed on the first sweep for $[s_N, s_{N-1}] = [0.5, 0.6]$. We compute the tail function

$$V^{(1)}(\mathbf{x}) = \frac{\ln w\left(\mathbf{x},\overline{s};\varepsilon_r^{(1)}\right) - \ln w_0(z,s)}{\overline{s}^2},\ \overline{s} = 1.2,$$

where $w\left(\mathbf{x},\overline{s};\varepsilon_r^{(1)}\right)$ is the solution of the problem (6.158), (6.160) with $\varepsilon_r := \varepsilon_r^{(1)}(x)$. Next, we set $V_{1,1}^{(2)}(x) := V^{(1)}(x)$ and repeat the algorithm of Sect. 6.4. We have made these sweeps until either

$$\left\|\varepsilon_r^{(p)} - \varepsilon_r^{(p-1)}\right\|_{L_2(\Omega_{P_2})} \leq 10^{-5}$$

or the gradient of the QRM functional has "exploded," i.e., when

$$\left\|\nabla J^{\alpha}_{n,k}\left(q^{(p)}_{n,k}\right)\right\|_{L_2(\Omega_{P_2})} \geq 10^5$$

for any appropriate indices n, k, p. Here, we use the discrete $L_2(\Omega_{P_2})$ norm. Tails were computed via solving the problem (6.158), (6.160) for $s := \overline{s}$.

The above algorithm has provided us with the function $\overline{\varepsilon}_{r,\text{glob}}(\mathbf{x})$. Next, we have found points $\{a_i\}$ of local maxima of this function and truncated the threshold as

$$\varepsilon_{r,\text{glob}}(\mathbf{x}) = \begin{cases} \overline{\varepsilon}_{r,\text{glob}}(\mathbf{x}), & \text{if } \overline{\varepsilon}_{r,\text{glob}}(\mathbf{x}) \geq 0.85\overline{\varepsilon}_{r,\text{glob}}(a_i), \\ 1 & \text{otherwise.} \end{cases} \tag{6.163}$$

This truncation was done in neighborhoods of points $\{a_i\}$. We note that such truncations are quite common in the image processing.

We have observed in our computations that the above algorithm can accurately image locations of mine-like targets. However, values of the function $\varepsilon_{r,\text{glob}}(\mathbf{x})$ near points of local maxima were not imaged accurately. Thus, we have applied a two-stage numerical procedure. While the first stage was the one described above, on the second stage, we have minimized the Tikhonov regularization functional via the gradient method taking the function $\varepsilon_{r,\text{glob}}(\mathbf{x})$ as the starting point. This was done similarly with Sect. 5.8.4. However, while in Sect. 5.8.4, we have applied the gradient method alone and were not successful, now we have applied it on the second stage only. Hence, unlike Sect. 5.8.4, we were successful this time. The latter indicates the importance of the first stage. When applying the gradient method, we have truncated as threshold 87.5% of maximal values on each iteration of the gradient method in a neighborhood of each point of local maxima $\{a_i\}$ of the function $\varepsilon_{r,\text{glob}}(\mathbf{x})$, similarly with (6.163).

6.8.4 Numerical Results

We refer to Fig. 6.1 for the schematic diagram of data collection. In both tests below, the incident plane wave falls from the top, and measurement data are also collected on the top side of this rectangular prism. Although only the 3D case is depicted on Fig. 6.1, the 2D case is similar.

Test 1. We test our numerical method for the case of two squares with the same size $p = 1$ of their sides. In the left square $\varepsilon_r = 6$, in the right one $\varepsilon_r = 4$, and $\varepsilon_r = 1$ everywhere else; see (6.161). Centers of these squares are at points $(-1.5, 0.6)$ and $(1.5, 1)$. However, we do not assume a priori in our algorithm neither the presence of these squares nor a knowledge of $\varepsilon_r(\mathbf{x})$ at any point of the square Ω. We took the initial tail for the function $\widehat{v}(\mathbf{x}, s)$ in (6.162) as $\widehat{V}_{1,1}(\mathbf{x}, s) \equiv 0$. Figures 6.2a and 6.2b display correct and computed images, respectively. Locations of both mine-like targets are images accurately. The computed function $\varepsilon_{r,\text{comp}}(\mathbf{x}) = 1$ outside of imaged inclusions. Next,

$$\max\left[\varepsilon_{r,\text{comp}}(\mathbf{x})\right] = \begin{cases} 6 \text{ in the left inclusion,} \\ 4.3 \text{ in the right inclusion.} \end{cases}$$

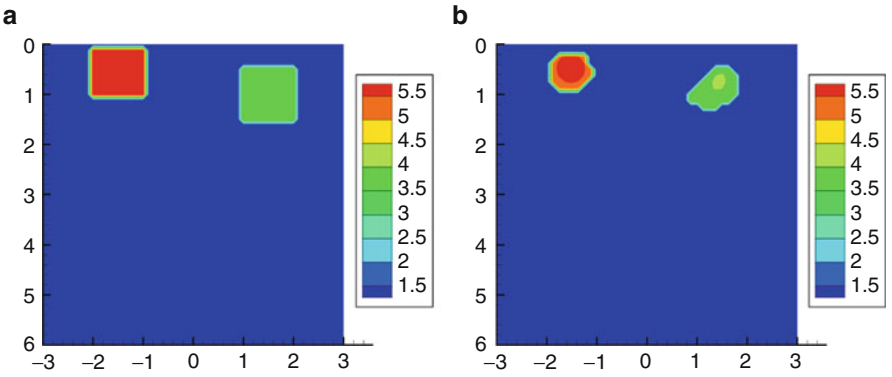

Fig. 6.2 Test 1. (**a**) Correct image. (**b**) Computed image. Locations of both mine-like targets are accurately imaged. The computed function $\varepsilon_{r,\text{comp}}(\mathbf{x}) = 1$ outside of imaged inclusions. The maximal value $\max \varepsilon_{r,\text{comp}}(\mathbf{x}) = 6$ in the left and $\max \varepsilon_{r,\text{comp}}(\mathbf{x}) = 4.3$ in the right imaged inclusion. Thus, the error in the inlcusion/background contrast is 0% in the left and 7% in the right imaged inclusion. The noise in the data was 5%. Source: A.V. Kuzhuget, N. Pantong and M.V. Klibanov, A globally convergent numerical method for a coefficient inverse problem with backscattering data, *Methods and Applications of Analysis*, 18, 47–68, 2011. Reprinted with permission

The error in the computed contrast in the right inclusion is 7%. Recall that the noise in the data was 5%. Therefore, inclusions/background contrasts are imaged accurately.

Test 2. The 3D Case. We have used 3D analogs of mine-like targets of Test 1. The size of the side of each of small cubes of Fig. 6.3a is $p = 1$. In the left cube, $\varepsilon_r = 6$, and in the right cube, $\varepsilon_r = 4$. Also, $\varepsilon_r = 1$ everywhere else. The distances between the centers and the upper side of the rectangular prism Ω were 0.6 in the left cube and 1 in the right cube. An obvious 3D analog of the problem (6.158), (6.160) was solved to simulate the backscattering data on the upper side $\{z = 0\}$ of the rectangular prism Ω of Fig. 6.3a:

$$\Omega = (-1.5, 1.5) \times (-3, 3) \times (0, 6).$$

The 5% noise in the data was introduced then, as in Sect. 6.8.3 . Although the data were simulated in 3D, when solving the inverse problem, we have solved twenty-three (23) 2D inverse problems in twenty-three (23) uniformly distributed vertical 2D cross-sections $\{x_i = b_i\}_{i=1}^{23}$ of the prism Ω.

We have solved them simultaneously on twenty-three (23) processors. We have done so because the QRM works slower in the 3D case than in the 2D case. In each 2D cross-section, the initial tail function was computed using the QRM solution of the problem (6.99), (6.100) and formula (6.101). We again have used (6.162). The above two-stage numerical method was applied. On the first stage, the approximately globally convergent numerical method of this chapter was applied. On the second stage, the gradient method of the minimization of the Tikhonov

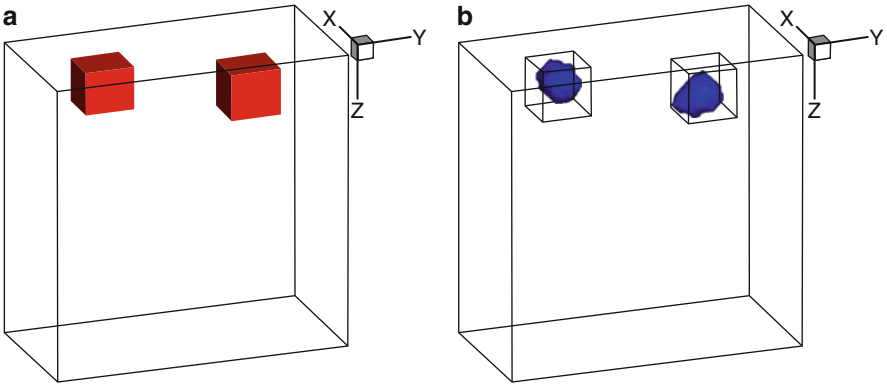

Fig. 6.3 Test 2. 3D case. (**a**) Correct image. (**b**) Computed image. Locations of both mine-like targets are accurately imaged. The computed function $\varepsilon_{r,\text{comp}}(\mathbf{x}) = 1$ outside of imaged inclusions. The maximal value $\max \varepsilon_{r,\text{comp}}(\mathbf{x}) = 6$ in the left and $\max \varepsilon_{r,\text{comp}}(\mathbf{x}) = 4$ in the right inclusion. Hence, the inclusion/background contrast is imaged very accurately for both inclusions

functional was used (Sect. 5.8.4). Having images in those 2D cross-sections, we have formed the 3D image then; see Fig. 6.3b. Locations of both inclusions are imaged accurately on this figure. The computed function $\varepsilon_{r,\text{comp}}(x) = 1$ outside of imaged inclusions. Also,

$$\max\left[\varepsilon_{r,\text{comp}}(x)\right] = \begin{cases} 6 \text{ in the left inclusion,} \\ 4 \text{ in the right inclusion.} \end{cases}$$

Therefore, inclusions/background contrasts are imaged very accurately.

6.8.5 *Backscattering Without the QRM*

A natural question to pose is *can the coefficient inverse problem 6.2 with the backscattering data (6.10) be solved by the approximately globally convergent algorithm of Sect. 2.6.1?* We now briefly describe in Test 3 one numerical example indicating that the answer on this question might be positive. This example was obtained just before submission of the text of this book to the publisher. Hence, although this example is promising, the corresponding study is not complete yet.

Test 3. In this test, the 2D analog of the coefficient inverse problem 6.2 is considered. However, the Neumann boundary condition $g_1(x,t)$ in (6.10) is not used. The data for the CIP were computationally simulated via solving the problem (6.155), (6.156) in a truncated domain, similarly with solving such problem in Sect. 4.17.1. To solve the forward problem (6.155), (6.156), we use the hybrid FEM/FDM method as in above chapters. The computational domain for the forward problem

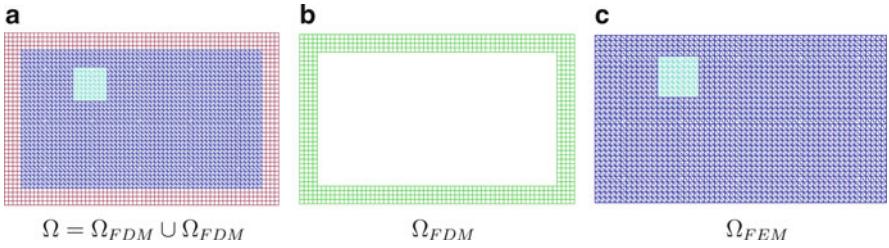

Fig. 6.4 (**a**) Geometry of the hybrid mesh. This is a combination of the quadrilateral mesh in the subdomain Ω_{FDM} (**b**), where we apply FDM, and the finite element mesh in the inner domain Ω_{FEM} (**c**), where we use FEM. The solution of the inverse problem is computed in Ω_{FEM}. The trace of the solution of the forward problem (6.155)–(6.156) is recorded at the top boundary Γ_1 of the finite element domain Ω_{FEM}

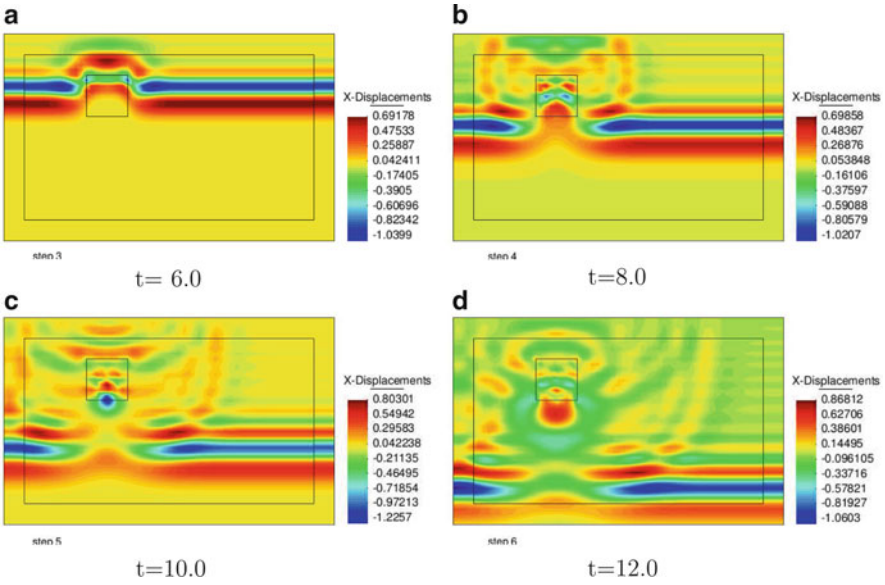

Fig. 6.5 Isosurfaces of the simulated exact solution for the forward problem (6.155)–(6.156) at different times with a plane wave initialized at the top boundary

is $\Omega = [-4, 4] \times [-1, 4]$; see Figs. 6.4 and 6.5. This domain is split into a finite element subdomain $\Omega_{\text{FEM}} := [-3.5, 3.5] \times [-0.5, 3.5]$ and a surrounding region Ω_{FDM} with a structured mesh such that $\Omega_{\text{FEM}} \cup \Omega_{\text{FDM}}$. The spatial mesh in Ω_{FEM} consists of triangles, and the mesh in Ω_{FDM} consists of squares. In the overlapping regions, the mesh size is $\widetilde{h} = 0.125$. The trace of the solution of the forward problem is recorded at the top boundary Γ_1 of Ω_{FEM}. This represents the backscattering data in space and time, and our goal is to reconstruct the unknown coefficient $\varepsilon_r(x)$ in (6.155) from these data inside the domain Ω_{FEM}.

In this test, when solving (6.26) for functions $q_{n,k}$, the function $\chi_2(x)$ was not used, and boundary conditions (6.28) were replaced with the following Dirichlet boundary conditions:

$$q_{n,k}|_{\Gamma_1} = \tilde{\psi}_{0,n}(x),\ q_{n,k}|_{\Gamma_2 \cup \Gamma_3} = \psi_{0,n}^{unif}(x). \tag{6.164}$$

Here functions $\tilde{\psi}_{0,n}(x)$ are obtained from functions $\psi_{0,n}(x)$ by setting them to zero outside of dents depicted on Figs. 6.6a, b. The functions $\psi_{0,n}^{unif}(x)$ are the ones which correspond to the case of the uniform background outside of the domain Ω_{FEM}. Recall that by (6.3) $c(x) = 1$ outside of Ω. Indeed, we have observed in our computational simulations that values of the function $\psi_0(x)$ on lateral sides of the rectangle Ω_{FEM} are only very slightly influenced by the presence of inclusions. And values of $\psi_0(x)$ on the bottom side of Ω_{FEM} are very close to zero.

Figure 6.6 displays the computed function $q(x,s), x \in \Gamma_1$ for different values of the pseudo-frequency s. We have started computations of the function $q(x)$ from very large values of the pseudo frequency $s = 18$ and finished with small values $s = 2$. We have observed numerically that the behavior of the function $|q(x,s)|$ for $x \in \Gamma_1$ is similar for all pseudo frequencies $s \leq 5$. Namely, this function is close to its maximal value only on a small part of the backscattering side Γ_1; see Fig. 6.4. This part of the boundary corresponds to the backscatered data from the inhomogeneity which should be reconstructed. However, all values of the function $|q(x)|$ for $s > 5$ are very close to zero; see Fig. 6.4e, f. Based on Fig. 6.7a–f, we have chosen the pseudo frequency interval for solving the inverse problem as $s \in [2,3]$. The grid step size with respect to s was $h = 0.05$. Just as in Sect. 5.7, we have used derivatives of tails $\partial_{\overline{s}} V_{n,k}(x,\overline{s})$ instead of tails themselves when computing functions $q_{n,k}$; see (2.182), (5.23), and Sect. 2.8.4 for explanations.

The algorithm of Sect. 2.6.1 was used to calculate the images of Fig. 6.7. Unlike Tests 1 and 2 in Sect. 6.8.4, the gradient method of the minimization of the Tikhonov functional was not used here. In other words, only the first stage of our two stage numerical procedure was used here. Location of the mine-like target is imaged accurately. Also, $\varepsilon_{r,\text{comp}}(x) = 1$ outside of the imaged inclusion, which is the correct value. Finally, $\max\left[\varepsilon_{r,\text{comp}}(x)\right] = 4$, which is the correct value. In other words, the inclusion/background 4 : 1 contrast is also accurately imaged.

6.9 Blind Experimental Data Collected in the Field

In this section, we present results which were obtained for the case of **blind** experimental data collected by the forward looking radar of US ARL [126]. We have obtained five (5) pieces of experimental data. Two of them are described here, and three more will be described in the paper [117]. All five cases were treated by exactly the same technique and accurate solutions were obtained for all of them.

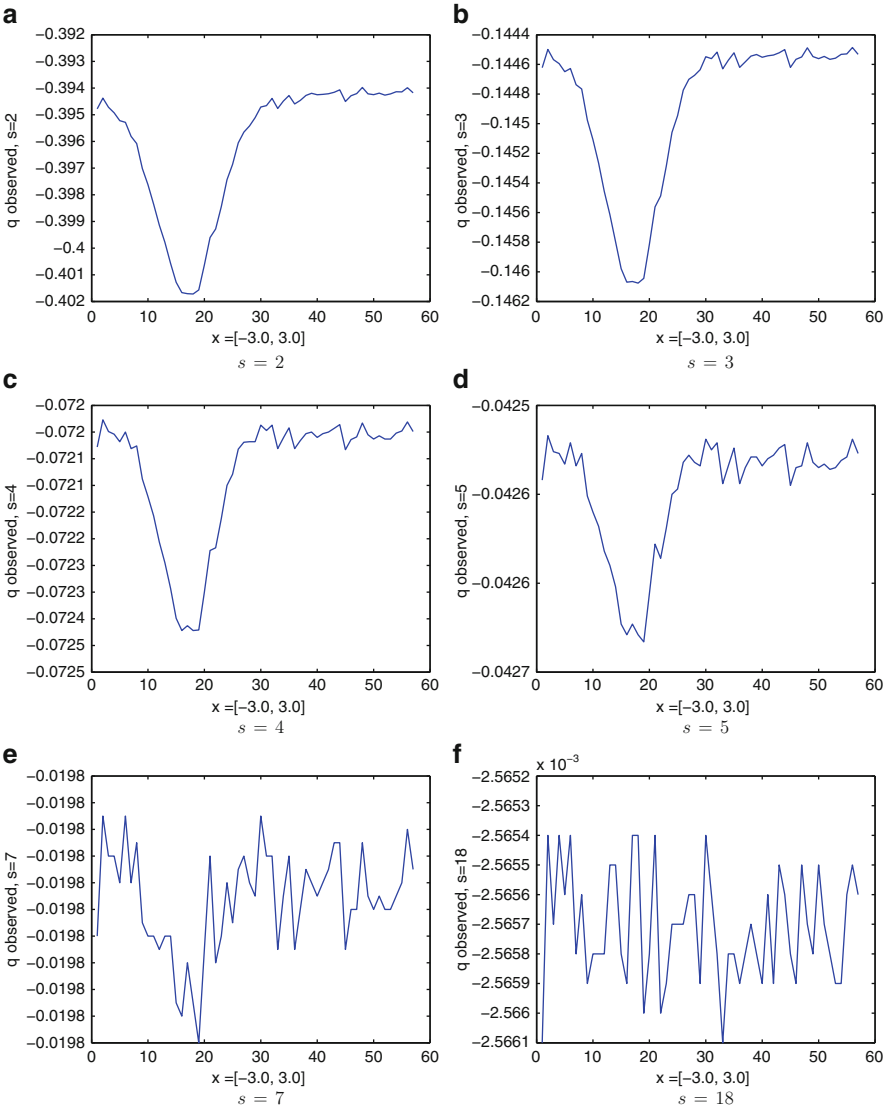

Fig. 6.6 Backscattered data for the function q at the top boundary Γ_1 of the computational domain Ω_{FEM} computed for the different values of the pseudo frequency s. We observe that for all pseudo frequencies $s \leq 5$, the values of the function $|q(x,s)|$ are close to its maximal value only on a small part of the boundary Γ_1. Values of the function $q(x,s)$ at the rest of Γ_1 are close to a constant. At the same time, $|q(x,s)| \approx 0, x \in \Gamma_1$ for $s > 5$. Computations were peformed with the software package WavES [148]

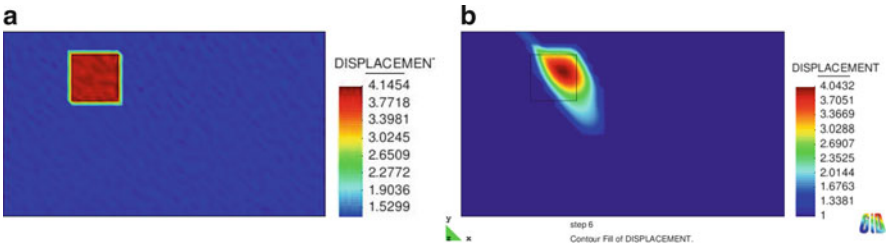

Fig. 6.7 (**a**) The computed image of the function $\varepsilon_{1,1}$ using backscattered data obtained from the geometry presented on Fig. 6.4a. Here, we used the exact tail and the variational formulation (3.14) for computing the function $\varepsilon_{1,1}$. (**b**) Computed image using backscattered data obtained from the geometry presented on Fig. 6.4a. Both location and contrast of the inclusion are accurately imaged. The computed function $\varepsilon_r = 1$ outside of imaged inclusions. The noise level in data is 5%

6.9.1 Introduction

The term "**blind**" means here that the mathematical sub-team of the authors of [117] (A.V. Kuzhuget, L. Beilina and M.V. Klibanov) had only two pieces of information when computing. The first piece was that only one target per data set was in place. And the second piece was where that target was located: below or above the ground. However, the mathematical team did not know neither constituent materials of targets, their sizes and locations, their dielectric constants nor soil. The engineering sub-team of the authors of [117] (L. Nguyen and A. Sullivan) knew the complete information about both the background medium and the targets. However, they have revealed this information to mathematicians only after computational results were presented to that team. In particular, it was revealed that the ground was always the dry sand with the dielectric constant in it:

$$\varepsilon_r \text{ (ground)} \approx 3; \tag{6.165}$$

see [151] as well as Figs. 6.14a and 6.16a. However, this dielectric constant was not measured directly, but rather was taken from tables [151].

Since dielectric constants of both targets and soil were not measured at the time when experimental data were collected, computed dielectric constants were a posteriori compared with tabulated values for constituent materials of those targets [151]. This comparison has revealed a good accuracy of computational results; see below.

A peculiar question is *how to interpret the dielectric constant of a metallic target*? This question is addressed on Figs. 6.8a, b, which were computed by Dr. Michael A. Fiddy. Comparison of these two figures shows that metallic targets can be viewed as dielectric targets with large values of dielectric constants. Hence, we choose

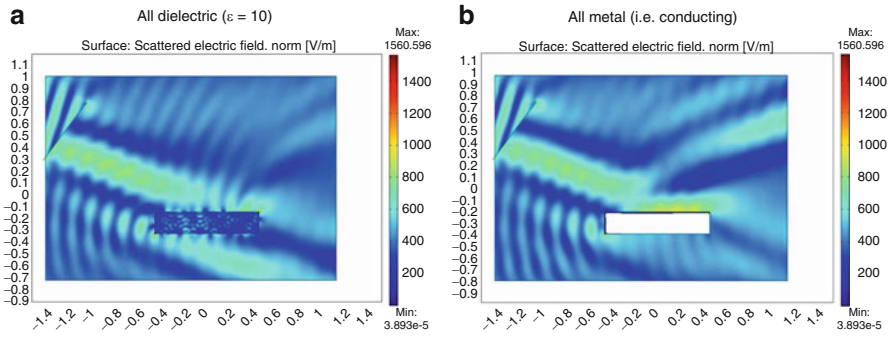

Fig. 6.8 Comparison of the reflected electric waves from a piece of metal and from a piece of dielectric with a large value of the dielectric constant. Only a single frequency is used. On (**a**) dielectric target with $\varepsilon_r = 10$ and on (**b**) metallic target are shown. Comparison of these two figures shows that reflected fields are very similar. Therefore, a metallic target can be viewed as a dielectric target with a large value of the dielectric constant ε_r

the following interpretation, which is only a conditional one and has no physical meaning:

$$\varepsilon_r(\text{metal}) \geq 10. \tag{6.166}$$

We call this *conditional dielectric constants* for metals. Furthermore, our computational simulations (not shown here) have demonstrated that values of the backscattering data $\varphi(s) := w(0, s)$ in (6.179) were changing only slightly when the value of ε_r (target) has increased larger than 10. Therefore, it is unlikely that target/background contrasts exceeding 10 can be accurately imaged.

6.9.2 *Data Collection and Imaging Goal*

The schematic diagram of data collection by the forward looking radar is depicted on Figs. 6.9 and 6.10. The goal of this radar is to detect and possibly identify shallow mine-like targets under the ground (a few centimeters depth) as well as those lying on the ground. The signals are originated by electric pulses emitted by two sources installed on the radar with 2 meters distance between sources. Only one component of the electric field is originated by these pulses. The time dependence of that component of the electric field is measured in the backscattering regime. Measurements are performed by sixteen (16) detectors with the step size in time of 0.133 nanosecond. For any target of interest, the radar/target distance is provided by the ground positioning system (GPS) in real time with only a few centimeters error.

For a shallow target which is located either above the ground or a few centimeters deep under the ground, the GPS provides the distance between the radar and a point on the ground located above that target. Resulting time-dependent curves are

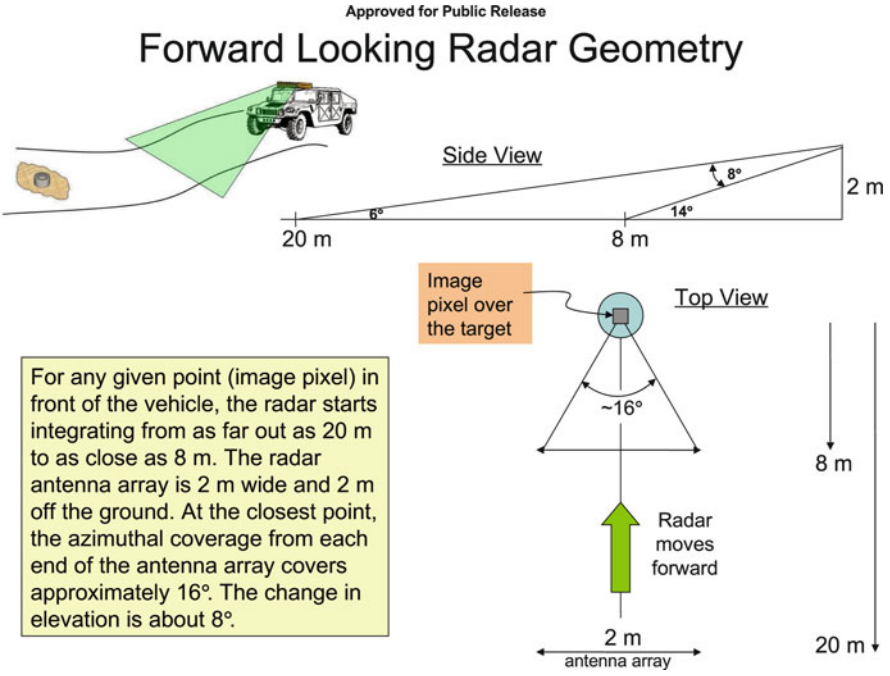

Fig. 6.9 The schematic diagram of data collection by the forward looking radar of US Army Research Laboratory

integrated over radar/target distances between 20 meters and 8 meters. In addition, readings of all sixteen (16) detectors are averaged. Hence, for any target of interest, only a single time dependent curve, which was approximately "responsible" for this target, was given to us. This means in turn that only a 1D CIP can be solved.

Since the radar/target distance is provided by GPS with a good accuracy, geometrical parameters of targets, including their depths, are not of an interest here. On the other hand, the available data processing procedure of this radar delivers only the energy information. Hence, the *main goal* of our work was to provide an additional imaging capability for this radar via imaging ratios R of dielectric constants:

$$R = \frac{\varepsilon_r(\text{target})}{\varepsilon_r(\text{background})}. \tag{6.167}$$

Using (6.165) and the value of R in (6.167), one can easily calculate ε_r(target) for targets located under the ground. In the case when the target is located above the ground, we have

$$\varepsilon_r\ (\text{background}) = \varepsilon_r\ (\text{air}) = 1.$$

Hence, $R = \varepsilon_r$(target) for targets located above the ground. Since targets can be mixtures of constituent materials, then ε_r(target) is a certain weighted average of dielectric constants of these materials.

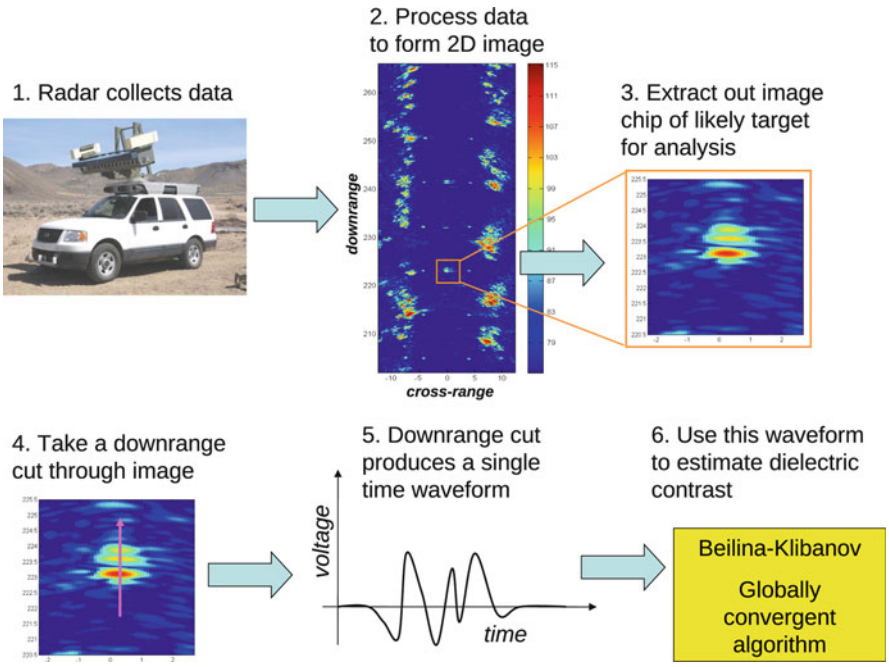

Fig. 6.10 The experimental setup for backscattered data collected in the field by a radar of the US Army Research Laboratory

We have imaged the ratio (6.167) rather than the function $\varepsilon_r(x)$ itself because one of conditions of our theory is that the unknown coefficient should have a known constant value outside of the domain of interest Ω; see (6.3). In our mathematical model, $\Omega = (0,1)$, where "1" stands for 1 meter. The point $x = 0$ corresponds to the ground, and $\{x < 0\}$ corresponds to the air in our mathematical model. We have assumed that $\varepsilon_r(x) = 1$ for $x \notin \Omega$. However, since the sand is not dry on the depth exceeding one meter, then (6.165) is invalid for $x > 1$. Also, values of ε_r(background) were not measured, but rather were taken from tables [151]. Hence, computing the ratio R in (6.167) was preferable.

6.9.3 The Mathematical Model and the Approximately Globally Convergent Algorithm

Since we were given only one time resolved curve for each target, we had no choice but to solve a 1D CIP. We have modeled the process by the 1D analog of the forward problem (6.1), (6.2). Following (6.167), let

$$\overline{\varepsilon}_r(x) := R(x) = \frac{\varepsilon_r(\text{target})}{\varepsilon_r(\text{background})}(x), \ x \in \mathbb{R}, \tag{6.168}$$

meaning that $R(x)$ is a function. The forward problem is

$$\overline{\varepsilon}_r(x) u_{tt} = u_{xx}, \ x \in \mathbb{R}, \ t \in (0, \infty), \tag{6.169}$$

$$u(x,0) = 0, u_t(x,0) = \delta(x - x_0), \ x_0 = \text{const.} < 0. \tag{6.170}$$

We assume that

$$\overline{\varepsilon}_r(x) \geq \varepsilon^0 = \text{const.} 0, \forall x \in \mathbb{R}, \tag{6.171}$$

$$\overline{\varepsilon}_r(x) \in \left[\varepsilon^0, d\right], \tag{6.172}$$

where $d = \text{const.} > 1$. Also, we assume that

$$\overline{\varepsilon}_r(x) = 1, x \notin (0,1). \tag{6.173}$$

Thus, the interval $\Omega := (0,1)$ is our domain of interest. One of complicating factors was that neither the "zero time" nor the source/medium distance were not given to us, i.e., the source position x_0 in (6.170) was not given. Indeed, it is unclear from Fig. 6.9 what kind of the distance is between the source and the domain of interest. We purely intuitively set in (6.170)

$$x_0 := -1. \tag{6.174}$$

Hence, we have assumed that the source is 1 meter away from the domain of interest. As always, we use the source position outside of the interval of interest $(0,1)$ because our technique works only with this case. We consider the following:

Coefficient Inverse Problem 6.9.3. *Suppose that the following function $\varphi(t)$ is known*:

$$u(0,t) = g(t), t \in (0, \infty). \tag{6.175}$$

Given conditions (6.169), (6.170), (6.171), (6.172), (6.173), and (6.174), determine the function $\overline{\varepsilon}_r(x)$ for $x \in (0,1)$.

Hence, the function $g(t)$ models the backscattering data measured by the forward looking radar. To solve this inverse problem, we have applied the 1D version of the approximate globally convergent method of this chapter. Thus, the 1D version of the QRM was applied. Since the convergence analysis in 3D was done above, we do not present it here. We refer to [114] for details of both the convergence analysis in the 1D case and for the numerical implementation.

As it was mentioned in Sect. 6.8.3, in 2D and 3D cases, we have applied the two-stage numerical procedure. On the second stage, the Tikhonov functional was minimized as described in Sect. 5.8.4. However, we have observed that the

application of the second stage to these experimental data has resulted in rather small changes of solutions. Hence, we have used only the first stage.

In terms of the above notations, we have in the 1D case

$$\Gamma_1 = \{x = 0\}, \ \Gamma_2 = \varnothing, \ \Gamma_3 = \{x = 1\}.$$

Hence, it seems to be that each boundary value problem (6.26), (6.28) can be treated in the 1D case as the conventional Sturm–Liouville problem for the function $q_{n,k}$. To do this, one needs to ignore in (6.28) either Dirichlet or Neumann boundary condition at Γ_1 and use two remaining boundary conditions (6.28): one at Γ_1 and the second one at Γ_3. However, our attempt to follow this path did not lead to acceptable quality solutions for computationally simulated data; see p. 126 of [114]. This indicates that the QRM is probably the optimal choice for the 1D case.

Just as above, consider the Laplace transform:

$$w(x,s) = \int_0^\infty u(x,t)\, e^{-st} dt, \ s \geq \underline{s} = \text{const.} > 0, \tag{6.176}$$

where $u(x,t)$ is the solution of the problem (6.169), (6.170). Then

$$w_{xx} - s^2 \overline{\varepsilon}_r(x)\, w = -\delta(x - x_0), \ x \in \mathbb{R}, \tag{6.177}$$

$$\lim_{|x| \to \infty} w(x,s) = 0. \tag{6.178}$$

In addition, by (6.175) and (6.176),

$$w(0,s) = \varphi(s), \tag{6.179}$$

where $\varphi(s)$ is the Laplace transform of the function $g(t)$. However, to apply the QRM, we also need to know the derivative:

$$w_x(0,s) = \rho(s). \tag{6.180}$$

To find the function $\rho(s)$, consider first the function $w_0(x,s)$ which is the solution of the problem (6.177), (6.178) for the case $\overline{\varepsilon}_r(x) \equiv 1$:

$$w_0(x,s) = \frac{\exp(-s|x - x_0|)}{2s}.$$

Let $\overline{w}(x,s) = w(x,s) - w_0(x,s)$. Then (6.177)–(6.179) imply that

$$\overline{w}_{xx} - s^2 \overline{\varepsilon}_r(x)\, \overline{w} = s^2 (\overline{\varepsilon}_r(x) - 1) w_0, \ x \in \mathbb{R}, \tag{6.181}$$

$$\lim_{|x| \to \infty} \overline{w}(x,s) = 0, \tag{6.182}$$

$$\overline{w}(0,s) = \overline{\varphi}(s) := \varphi(s) - \frac{\exp(-s|x_0|)}{2s}. \tag{6.183}$$

Since by (6.173) $\overline{\varepsilon}_r(x) = 1$ for $x < 0$, then (6.181), (6.182), and (6.183) become for $x < 0$:

$$\overline{w}_{xx} - s^2\overline{w} = 0, \ x < 0, \tag{6.184}$$

$$\lim_{x\to-\infty} \overline{w}(x,s) = 0, \tag{6.185}$$

$$\overline{w}(0,s) = \overline{\varphi}(s). \tag{6.186}$$

We can consider (6.184), (6.185), and (6.186) as the boundary value problem on the half line $\{x < 0\}$. Obviously, the unique solution of this problem is

$$\overline{w}(x,s) = \overline{\varphi}(s) e^{sx}, \ x < 0.$$

Hence,

$$\overline{w}_x(0,s) = s\overline{\varphi}(s).$$

Next, $w_x(0,s) = \overline{w}_x(0,s) + w_{0x}(0,s)$. Since by (6.174) $x_0 < 0$, then by (6.180),

$$w_x(0,s) := \rho(s) = s\varphi(s) - \exp(-s|x_0|). \tag{6.187}$$

Therefore, both functions $w(0,s)$ and $w_x(0,s)$ are known, which are required by the QRM. Also, since $\overline{\varepsilon}_r(x) = 1$ for $x > 1$, then (6.177) and (6.178) imply that

$$w(x,s) = C(s) e^{-sx}, x > 1,$$

where $C(s)$ is a certain function of s. Using

$$q(x,s) = \frac{\partial}{\partial s}\left(\frac{\ln w(x,s)}{s^2}\right),$$

we obtain the following analog of the boundary condition (6.29):

$$q_x(1,s) = \frac{1}{s^2}. \tag{6.188}$$

Boundary conditions (6.180), (6.187), and (6.188) were used to obtain 1D analogs of boundary conditions (6.28).

Just as in (6.162), we have replaced functions $v(x,s)$, $q(x,s)$,

$$v(x,s) = \frac{\ln[w(x,s)]}{s^2}, \ q(x,s) = \partial_s v(x,s),$$

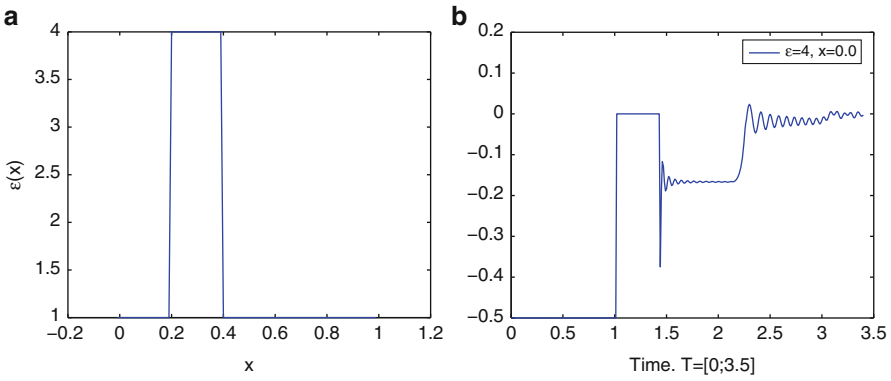

Fig. 6.11 (**a**) The medium with a single target and $\overline{\varepsilon}_r(x) = 4 > 1$ within this target. (**b**) The computed function $g(t) = u(0,t) - u_0(0,t)$ for a). Here, $u(x,t)$ is the solution of the problem (6.169), (6.170) for the function $\overline{\varepsilon}_r(x)$ depicted on (a), and $u_0(x,t)$ is the solution of the problem (6.169), (6.170) for the case $\overline{\varepsilon}_r(x) \equiv 1$

with functions $\widehat{v}(x,s)$, $\widehat{q}(x,s)$, where

$$\widehat{v}(x,s) = \frac{1}{s^2} \ln\left[\frac{w}{w_0}(x,s)\right], \ \widehat{q}(x,s) = \partial_s \widehat{v}(x,s). \tag{6.189}$$

This led to obvious modifications of (6.26) and (6.28).

To approximate tails, one should solve the problem (6.181), (6.182) at $s := \overline{s}$. Using (6.182), one can prove that the function $\overline{w}(x,s)$ decays exponentially as $|x| \to \infty$. Hence, we have solved the Sturm–Liouville problem for (6.181) in the interval $x \in (-4,6)$ with the boundary conditions

$$\overline{w}(-4,s) = \overline{w}(6,s) = 0.$$

6.9.4 Uncertainties

Similarly with the experimental data of Chap. 5, the data from the forward looking radar have **huge misfits** with computational simulations: Compare Fig. 6.12b with Fig. 6.13a as well as Fig. 6.11b with Fig. 6.15a. In addition, there are some other significant uncertainties here, which were not presented in experimental data of Chap. 5. These difficulties are basically caused by the fact that experimental data were collected in the field rather than in the controlled environment of a laboratory of Chap. 5. We now list those factors:

1. We did not have the reference signal for comparison.
2. The direction of the incident plane wave was oblique to the ground rather than orthogonal; see Figs. 6.14a and 6.16a.

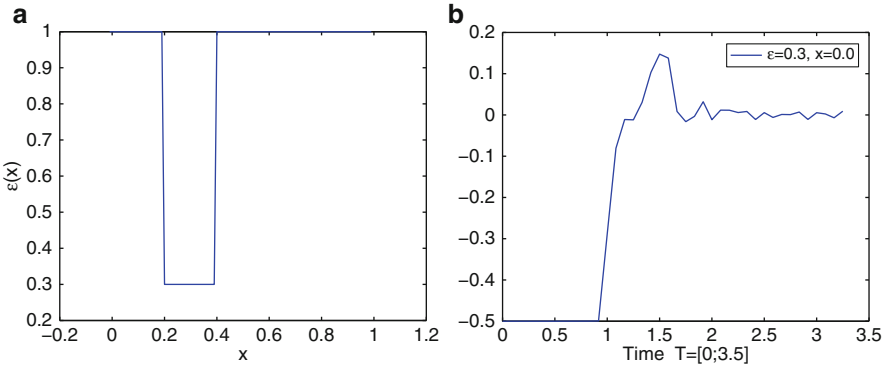

Fig. 6.12 (**a**) The medium with a single target and $\overline{\varepsilon}_r(x) = 0.3 < 1$ within this target. (**b**) The computed function $g(t) = u(0,t) - u_0(0,t)$ for (a). Here, $u(x,t)$ is the solution of the problem (6.169), (6.170) for the function $\overline{\varepsilon}_r(x)$ depicted on (a), and $u_0(x,t)$ is the solution of the problem (6.169), (6.170) for the case $\overline{\varepsilon}_r(x) \equiv 1$

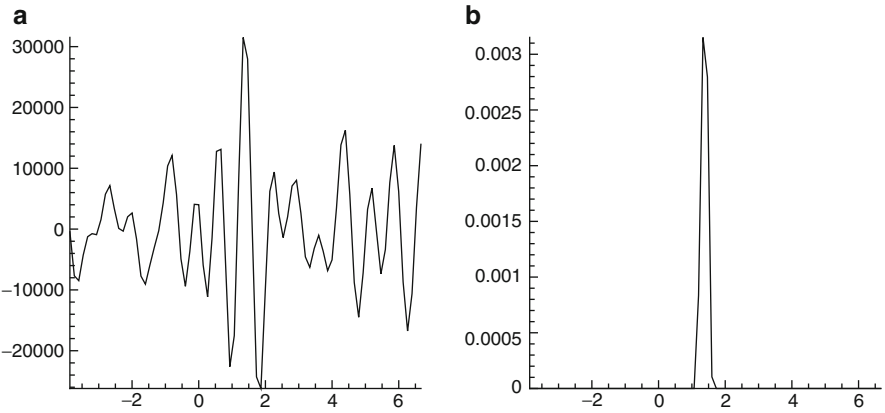

Fig. 6.13 Test 1. (**a**) A sample of the experimentally measured signal for a buried object depicted on Fig. 6.14a. It is unclear which part of this curve is responsible for this object and which part is responsible for the rest of the measured signal. Horizontal axis is time in nanoseconds. It is unclear where the time $t = 0$ is. It is also unclear which units are displayed on the vertical axis. (**b**) Pre-processed signal of (a). First, we have multiplied the amplitude of (a) by 10^{-7}. This multiplier was chosen to have about the same values of functions $w(0,s)$ in (6.179) for both simulated and experimental data. Next, we have selected the peak with the largest absolute value and have set the rest of the curve to zero. We set zero time $t = 0$ being 1 nanosecond to the left from the beginning of the selected peak. We apply our algorithm only to the data of (b)

3. We did not know the units for the amplitude of experimental data. These amplitudes were about $3 \cdot 10^4$, which is too large.
4. We did not know the source location. Thus, we have just intuitively assigned by (6.174) $x_0 := -1$.
5. We did not know where the time $t = 0$ was on the data.

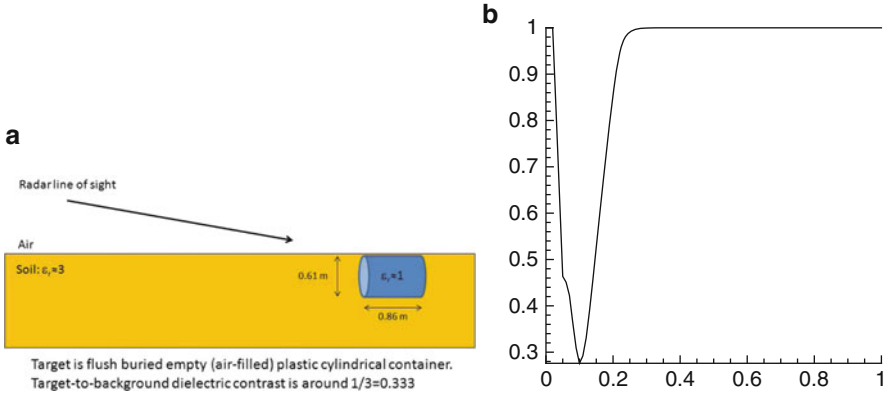

Fig. 6.14 Test 1. (**a**) The real image from which the data of Fig. 6.13a were collected. This is a buried plastic cylinder with $\varepsilon_r \approx 1$ in it; see [151]. (**b**) Computed 1D image of (a). Most importantly, $\min \overline{\varepsilon}_r = 0.28$, whereas the true value $\overline{\varepsilon}_r \approx 0.33$. Thus, a good accuracy in this blind imaging was achieved

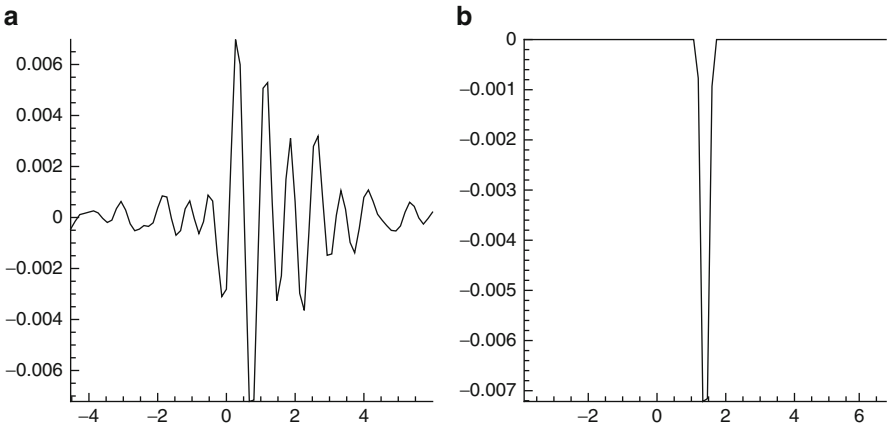

Fig. 6.15 Test 2. (**a**) The real signal. The amplitude was multiplied by 10^{-7}; see Sect. 6.9.4 for the data pre-processing procedure. (**b**) The pre-processed signal of (a)

6. We had only one time resolved curve for each target, whereas the reality is 3D.
7. We did not have a reference signal, unlike Chap. 5.
8. Since targets were surrounded by clutter, then the background was inhomogeneous. Targets might be heterogeneous ones as well. We remind that a knowledge of the background is not assumed in the approximately globally convergent method of this book.

At the same time, we had the following two simplifying factors:

A. We knew that the target is present and that we should work only with one target for each data set. In addition, we knew whether the target is located above the ground or buried in the ground.

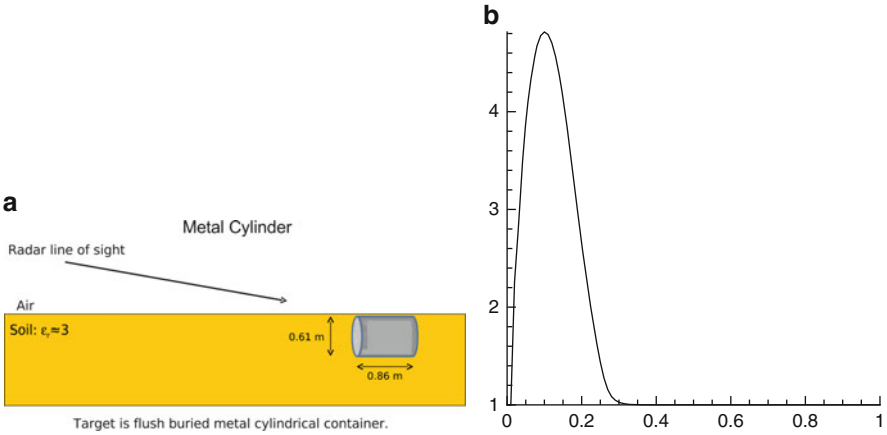

Fig. 6.16 Test 2. (**a**) The real image from which the data on Fig. 6.15a were collected. This is a buried metal box. (**b**) The computed 1D image of (a). Here, the maximal value of the target/background ratio of dielectric constants is $\max \overline{\varepsilon}_r = 4.8$. Hence, the computed value of the dielectric constant of this target is $\varepsilon_r = 4.8 \cdot 3 = 14.4$ which is about the right value of the apparent dielectric constants of metals; see Sect. 6.9.1. Therefore, a good accuracy in this blind imaging was achieved

B. We were not interested to image locations of targets. Furthermore, it was impossible to image locations accurately, since both the source position and the zero time were unknown. Rather, all what we wanted was to accurately compute either $\max \overline{\varepsilon}_r(x)$ or $\min \overline{\varepsilon}_r(x)$ within the target.

6.9.5 Data Pre-processing

As it was demonstrated in Chap. 5, it is crucial to pre-process experimental data in order to handle the abovementioned huge misfit between experimental and computationally simulated data. The idea of the data pre-processing procedure is similar with the idea of Chap. 5: basically, we immerse the experimental data in computationally simulated ones by using only one peak of the largest amplitude.

To figure out what kind of ideal data one should expect, we have performed computational simulations via solving the forward problem (6.169), (6.170), (6.174) for the case of one target. In data simulations, we have replaced $\mathbb{R}$ in (6.169) with the interval $x \in (-6, 6)$ and have set

$$u(-6, t) = u(6, t) = 0, t \in (0, 4). \tag{6.190}$$

Because of the structure of the medium, the signal did not yet reach points $x = \pm 6$ for $t \in (0, 4)$. This justifies boundary conditions (6.190). Figures 6.11 and 6.12

display two structures of the medium we have tested as well as the computed functions functions $g(t) = u(0,t) - u_0(0,t)$ for them. Here, $u_0(x,t)$ is the fundamental solution of the equation $v_{tt} = v_{xx}$,

$$u_0(x,t) = \frac{1}{2} H(t - |x - x_0|),$$

where H is the Heaviside function,

$$H(x) = \begin{cases} 1 \text{ if } x \geq 0, \\ 0 \text{ if } x < 0. \end{cases}$$

One can see from Figs. 6.11 and 6.12 that when working with one target only, one should anticipate only one peak in the backscattering data. We use this observation in our data pre-processing procedure.

Scaling

Figure 6.13a displays a typical sample of the experimental data we have worked with. First of all, the amplitude of the signal is too large, since its maximal value is $3 \cdot 10^4$. This is well above amplitudes of Figs. 6.11 and 6.12. Hence, we need to scale this signal via multiplying these data by a small number. A natural question is about the value of this number. We have multiplied all experimental data by 10^{-7}. In this case, the magnitudes of the values of the function $w(0,s)$ in the experimental data were about the same as ones in computational simulations for small inclusions with reasonable contrasts.

The Largest Peak

It is unclear from Fig. 6.13a which part of the signal is responsible for reflections from the clutter, including the air/ground interface. On the other hand, we need to select such a part of the signal, which is responsible for reflections from the target. In other words, we now have the same problem as the one we have faced in Chap. 5. We knew that the target might well be a heterogeneous one, especially since it is mixed with the ground. Nevertheless, one can hope to obtain only an average value of the function $\overline{\varepsilon}_r(x)$ within the target.

Based on Figs. 6.11 and 6.12, we have decided to select the peak of the largest amplitude out of all other peaks of Fig. 6.13a and set the rest of the curve to zero. We have done this for all five pieces of experimental data we had. Now, if the target is located above the ground, then $\overline{\varepsilon}_r(\text{target}) = \varepsilon_r(\text{target}) > 1$, since $\varepsilon_r(\text{air}) = 1$. Figure 6.11b tells one that the selected peak should look downward in this case.

Hence, our selection of the single peak was as follows: This should be the earliest peak of the largest amplitude:

$$\text{out of all} \begin{cases} \text{peaks for an underground target,} \\ \text{downward looking peaks for an above the ground target.} \end{cases} \tag{6.191}$$

Next, we regard the time zero: $\{t = 0\}$ as the point on the time axis, which is 1 nanosecond to the left from the beginning of the selected peak.

The Laplace Transform of the Pre-processed Data

To apply our algorithm, the Laplace transform (6.176) was calculated for the pre-processed time resolved data. It is clear from Fig. 6.13b that only the integration over a finite time interval is needed in this case. Since we also need to calculate the s-derivative of this transform, then we have used the formula

$$\varphi'(s) = -\int_0^\infty g(t)\, t e^{-st} \mathrm{d}t, \tag{6.192}$$

where $g(t)$ is pre-processed data and $\varphi(s)$ is its Laplace transform.

Just as in Sect. 6.8.3, we have observed in computational simulations of Figs. 6.11 and 6.12 that the function $\varphi(s)$ in (6.179) has the best sensitivity to the presence of inclusions for $s \in [0.5, 1.2]$. Still, we have discovered in our computational simulations that better to work on a larger interval $s \in [0.5, 12]$. However, in the case of the pre-processed experimental data, the function $q(0, s)$ was highly oscillatory for $s \in [5, 12]$.

Hence, we have pre-processed the function $\widehat{q}(0, s)$ in (6.189) as follows. First, we have calculated the function $\widehat{q}(0, s)$ for $s \in [0.5, 2.5]$ for the pre-processed experimental data using (6.192). Next, we have assigned

$$\widehat{q}(0, 12) := 0.025 \cdot \widehat{q}(0, 2.5).$$

Next, we have linearly interpolated in the plane $(s, \widehat{q})$ between points $(s_1, \widehat{q}_1)$ and $(s_2, \widehat{q}_2)$, where

$$(s_1, \widehat{q}_1) := (2.5, \widehat{q}(0, 2.5)), \quad (s_2, \widehat{q}_2) := (12, \widehat{q}(0, 12)).$$

Next, we have assigned to the function $\widehat{q}(0, s)$ those values for $s \in [2.5, 12]$, which were taken on this line after the linear interpolation. We have done the same to the function $\widehat{q}_x(0, s)$. For $s \in [0.5, 2.5]$, the function $\widehat{q}_x(0, s)$ was calculated using (6.179), (6.187), and (6.189). Derivatives with respect to s were calculated via finite differences. Thus, these values of functions $\widehat{q}(0, s)$, $\partial_x \widehat{q}(0, s)$ were used

to calculate 1D analogs of boundary conditions $\psi_{0,n}, \psi_{1,n}$ in (6.28):

$$\widehat{q}_n(0) = \widehat{\psi}_{0,n}, \ \partial_x \widehat{q}_n(0) = \widehat{\psi}_{1,n}.$$

Next, the 1D analog [114] of the algorithm of Sects. 6.4.3 and 6.4.4 was applied, and functions $\widehat{\psi}_{0,n}, \widehat{\psi}_{1,n}$ were the input data for this algorithm. The grid step size in the s-direction was $h = 0.5$.

6.9.6 *Results of Blind Imaging*

Test 1. The data are depicted on Fig. 6.13a and the pre-processed data are displayed on Fig. 6.13b. We only knew a priori that this was a target buried in the ground; see (6.191). Other features of this target were unknown to us when computing. Figure 6.14b displays our computed image. After this image was computed, Drs. L. Nguyen and A. Sullivan have compared our result with the reality and have sent Fig. 6.14a to us. The target was an empty plastic cylinder buried in the ground with the dielectric constant ε_r(plastic)≈ 1 [151]. The dielectric constant of the ground (dry sand) was as in (6.191), ε_r(background)≈ 3. We remind that this value was unknown to the mathematical team when computations were performed. One can see that our computed $\min \overline{\varepsilon}_{r,\text{comp}}(x) = 0.28$. At the same time, the real value was $\overline{\varepsilon}_r \approx 0.33$. Thus, our blindly computed result is quite accurate.

Test 2. The data, which were multiplied by 10^{-7} first (for scaling, see above), are depicted on Fig. 6.15a. We only knew a priori that this was a target buried in the ground. Other characteristics of this target were unknown to us at the time when computations were performed. Hence, following (6.191), we have selected on Fig. 6.15a the peak of the largest amplitude. Figure 6.16b displays our 1D computed image. Figure 6.16a depicts the real image, which was revealed to us by Drs. L. Nguyen and A. Sullivan only after the computational result was sent to ARL. The target was a metal box. One can see that our computed $\max \overline{\varepsilon}_r(x) = 4.8$. Since ε_r(ground)≈ 3, then the computed $\max \varepsilon_{r,\text{comp}}$(target)$\approx 3 \cdot 4.8 = 14.4$. This is the conditional dielectric constant of the metal box of Fig. 6.16b, see Sect. 6.9.1 for the definition of the conditional dielectric constant of metals. Hence, this result matches well Figs. 6.8a, b and (6.166).

Remark 6.9.6.

1. The sign "$\approx$" is used in this table instead of "$=$" because the values of the dielectric constant of the ground were only approximate ones, since they were not measured in experiments.
2. The value $\varepsilon_r = 0.84$ in Table 6.1 does not match physics well since $0.84 < 1$. However, the value ε_r(ground)≈ 3 is only an approximate one. If, for example, the real value was ε_r(ground)≥ 3.58, then the computed value ε_r of the target

Table 6.1 Summary of results of blind imaging of the data collected by the forward looking radar

Test number	Computed ε_r of the target	Tabulated ε_r
1 (buried plastic cylinder)	≈ 0.84	≈ 1
2 (buried metal cylinder)	≈ 14.4	≥ 10
3 (buried metal box)	≈ 11.4	≥ 10
4 (wood stake in air)	3.8	from 2 to 6
5 (bush: clutter in air)	6.4	from 3 to 20

was exceeding 1. Note that in tables [151], the dielectric constant of the dry sand is listed as being between 3 and 5. Hence, the most important point of the result of Test 1 is that the computed ratio $\min \overline{\varepsilon}_r(x) = 0.28$, which is quite close to the real value of about 0.33.

3. The computed conditional dielectric constant $\varepsilon_r \approx 14.4$ of the metal box is close to (6.166).

We had the blind data for five targets. Dielectric constants were not measured in experiments. Therefore, we had no choice but to compare our calculated values of dielectric constants of targets with tabulated ones [151]. In the case of bush we use the reference [52]. In the case of two metallic targets we use inequality (6.166). Table 6.1 summarizes our results.

6.9.7 Summary of Blind Imaging

It can be seen from the above description of complicating factors that we have worked with the case of a severely limited information caused by many uncertainties in the experimental data. Furthermore, we have worked with the most challenging case of blind experimental data. Nevertheless, above results demonstrate a surprisingly good accuracy. This is consistent with results of Chap. 5. Studies on larger sets of experimental data are necessary to figure out accuracy constraints of this algorithm.